The Use of Conduction Mode Basis Functions in Surface Integral Formulation for Wideband Impedance Extraction

by

Xin Hu

Submitted to the Department of Electrical Engineering and Computer Science
in partial fulfillment of the requirements for the degree of

Master of Science in Computer Science and Engineering

at the

MASSACHUSETTS INSTITUTE OF TECHNOLOGY

May 2003

©2003 Massachusetts Institute of Technology
All rights reserved

MASSACHUSETTS INSTITUTE OF TECHNOLOGY
JUL 07 2003
LIBRARIES

Author ....
Department of Electrical Engineering and Computer Science
May 9, 2003

Certified by.... .....
Jacob K. White
Professor
Thesis Supervisor

Accepted by .....
Arthur C. Smith
Chairman, Department Committee on Graduate Students

BARKER

The Use of Conduction Mode Basis Functions in Surface Integral Formulation for Wideband Impedance Extraction

by

Xin Hu

Submitted to the Department of Electrical Engineering and Computer Science
on May 9, 2003, in partial fulfillment of the
requirements for the degree of
Master of Science in Computer Science and Engineering

Abstract

This thesis presents an improved method of modeling contact current distribution in the quasi-static and full-wave surface integral equation solver FastImp [1]. A significant shortcoming of FastImp is its lack of a single uniform approach to model contact current across different frequencies. Its method of computing contact current at high frequencies does not efficiently and optimally capture skin and proximity effects. Its method of computing contact current at low frequencies lacks accuracy due to the use of a centroid collocation scheme when evaluating fields on the contact surfaces. The method discussed in this thesis offers a unified, more accurate and more efficient method of computing contact current over a wide range of frequencies. It is shown in this thesis that the electric field on the conductor contact surfaces can be modeled effectively by only a few conduction modes as basis functions. These conduction modes were first introduced in [2] for a "volume" integral equation solver. In this thesis, we improved these basis functions and adapted them into a "surface" integral equation solver. On the non-contact surfaces, the electric field is modeled by a set of standard piecewise constant basis functions. The surface-based conduction mode basis functions, used in a Galerkin technique, and the piecewise constant basis functions, used in a collocation scheme, are utilized for the discretization of the system of surface integral equations implemented in FastImp. Examples are used to validate the new method as an improvement from FastImp in its ability to compute contact current accurately, consistently and efficiently. The efficiency of the new method is demonstrated by its ability to use a significantly coarser surface discretization yet still managing to achieve comparable impedance accuracy in comparison to FastImp.

Thesis Supervisor: Jacob K. White
Title: Professor

Acknowledgments

The process of producing this thesis has been an incredibly rewarding experience in my life. Beyond the intellectual stimulation I have received from working on the thesis, it has been a personally enriching experience as well. I would like to express my sincere gratitude to all the people who have made this experience possible. Foremost is my advisor Jacob White, who has been an unlimited source of strength, knowledge and inspiration. Luca Daniel co-advised me on this thesis. I want to thank him for his amazing patience and even more amazing insights. I am grateful to both of my advisors for their unwavering faith in me, especially during the uncertain times when I was ready to give up.

Without Ben Song, Zhenhai Zhu and Junfeng Wang's ground-breaking work on the FastImp project, this thesis would never have been possible. I especially like to thank Ben and Zhenhai for their invaluable help which was imperative to the completion of my thesis work.

I am thankful that I belong to a lab with so many supportive members. They are not only my lab mates, they are my friends. I value their humor, their intellect and their generosity. They are: Annie Vithayathil, Jaydeep Bardhan, Dave Willis, Carlos Pinto Coelho, Dimitry Vasilyev, Jung Hoon Lee, Ben Song, Shihhsien Kuo, Dennis Wu, Tom Klemas, Michal Rewienski, and Zhenhai Zhu.

I would like to thank Chris LaFrieda for always being there for me and believing in me. Most importantly I want to express my gratitude towards my family, without whom I can never be where I am today. In conclusion, I would like to acknowledge the financial support from NDSEG fellowship in the past two years.

Contents

1 Introduction **11**

1.1 Motivation 11

1.2 Background 12

1.3 The problem 12

1.4 Overview 15

2 Surface integral formulation for full-wave impedance extraction **17**

2.1 First dyadic surface integral equation 18

2.2 Second dyadic surface integral equation 19

2.3 Scalar Poisson surface integral equation 21

2.4 Expression of current conservation as a surface integral equation . . . 21

2.5 Boundary conditions 22

2.6 Surface integral formulation summary 23

2.7 Impedance extraction 25

3 Basis functions for each type of unknowns **27**

3.1 Electric field 28

3.1.1 Conduction mode basis functions on contact surfaces 28

3.1.2 Piecewise constant basis functions on non-contact surfaces . . 32

3.1.3 Basis functions on the entire conductor surface 33

3.2 Surface normal derivative of the electric field 34

3.3 Surface charge density and electric potential 34

3.4 Basis functions summary 35

4 Discretization **37**

4.1 Discretization of the first dyadic surface integral equation 37

4.2 Discretization of the second dyadic surface integral equation 41

4.3 Discretization of the scalar Poisson surface integral equation [16] . . . 45

4.4 Discretization of the surface integral form of current conservation [16] 45

4.5 Discretization of boundary conditions 48

4.6 System formation 49

4.7 Current computation and impedance extraction 51

5 Computational results **53**

5.1 A straight wire 53

5.1.1 Accuracy 55

5.1.2 Cost 55

5.2 A ring 57

5.2.1 Accuracy 58

5.2.2 Cost 59

5.3 Transmission Line 59

5.3.1 Accuracy 60

5.3.2 Cost 60

5.4 Conclusion 61

List of Figures

1-1 A conductor structure 13

2-1 A system of conductors 17

2-2 A sample surface for current conservation 22

3-1 Volume discretization of a conductor with each section supporting a set of conduction mode basis functions. The arrow indicates the direction of current flow. 29

3-2 A side mode contact surface electric field distribution and its optimal contact area coverage. The arrow indicates the direction of current flow. 31

3-3 A corner mode contact surface electric field distribution and its optimal contact area coverage. 31

3-4 Electric field representation using all eight truncated conduction mode basis functions on a contact. 32

3-5 Conductor surface discretization for the electric field $\overline{E}$. 33

3-6 Conductor surface discretization for ϕ, ρ and $\frac{\partial \overline{E}}{\partial n}$. 35

4-1 Discretization of $\frac{\partial \phi}{\partial t_a}$ (a=1 or 2). 44

4-2 A dual panel 46

5-1 A discretized wire structure 54

5-2 Resistance of the wire 56

5-3 Inductance of the wire 57

5-4 A discretized ring structure 58

5-5 Resistance of the ring with a closer view of the "dip" in FastImp's results occurring at 100MHz due to the switching of contact current evaluation method. 62
5-6 Inductance of the ring 63
5-7 A discretized transmission line structure 63
5-8 Impedance amplitude vs. frequency for a shorted T-line plotted on a log amplitude scale. 64
5-9 Impedance amplitude vs. frequency for a shorted T-line plotted on a linear amplitude scale. 65
5-10 Impedance phase vs. frequency for a shorted T-line. 65

Chapter 1

Introduction

1.1 Motivation

As integrated circuits operate at increasingly higher speed, methods are needed that are capable of performing quasi-static and full-wave electromagnetic analysis over a wide range of frequencies, up to 10's of gigahertz (GHz). With this increase in frequencies, the assumption that lumped inductance and lumped capacitance can be extracted separately no longer holds true. Methods are needed that can take into account the effects of distributed resistive, capacitive and inductive impedance throughout the entire circuit layout in an accurate and efficient manner.

The importance of designing extraction tools capable of handling coupled parasitic effects is demonstrated by circuit interconnects. It is well known that parasitic capacitance and resistance of the interconnects can cause propagation delays, while their coupled inductance and capacitance can not only affect propagation delays, but also influence signal integrity [3]. For example, the coupling between two nearby interconnect wires or between an interconnect wire and the substrate introduces noise into their signals. In addition, the coupling of interconnects' inductance and capacitance can create resonance peaks in their frequency responses [4]. Thus it is imperative to have robust extraction tools that can recognize these parasitic effects during the designing stage of an integrated circuit layout so as to avoid costly post-prototype ad-hoc fixes, or even worse, the complete redesigning of the system.

1.2 Background

The development of accelerated integral equation solvers in the past decade has made the realization of aforementioned features feasible in electromagnetic analysis tools. Accelerated integral equation methods like those used in FastCap [5] and FastHenry [6], together with several techniques for handling skin and proximity effects [7, 8, 9, 10], enable detailed EM analysis of complicated integrated circuits to be performed in matter of minutes. More specifically, iterative methods such as GMRES [11] and matrix sparsification techniques such as fast multipole [6], Precorrected-FFT [12] and SVD algorithms [13] can reduce both CPU time and memory usage dramatically when solving a system of discretized integral equations.

Traditionally there have been two competing integral equation methods, one volume based and the other surface based. There are several advantages of surface methods over volume methods. One main advantage is that while volume based methods need to discretized the entire volume of a structure, surface methods only need to discretize the surface of the structure, thereby reducing the number of unknowns in the system [6]. In addition, discretization of a curved structure is handled with much more ease by surface methods than by volume methods.

1.3 The problem

The formulation described in this thesis addresses many issues currently plaguing the surface integral solver FastImp. One of the shortcomings of FastImp is that it switches between two different techniques of computing contact surface current depending on the operating frequencies applied to the conductor. Figure 1-1 shows the position of a contact in relation to a conductor. At low frequencies, FastImp evaluates contact current using a surface integral approximation that takes into account the sum of all the current flowing through the discretized panels on each contact. At high frequencies FastImp uses line integrations involving the magnetic field around the cross sections near the contacts to compute contact current. This abrupt change

of formulation from low frequencies to high frequencies breaks the continuity of the solution. However, the more obvious shortcomings of the FastImp algorithm are the issues encountered while performing impedance extractions at extreme frequencies. At low frequencies, FastImp's computation of impedance lacks accuracy due to its use of a centroid collocation scheme. At high frequencies, the formulation cannot adequately capture the current as it crowds near the sides and corners of a contact surface without using a much refined discretization that is computationally expensive. To make clear of this difficulty, consider that in order to capture skin and proximity effects accurately in FastImp, not only the dimension of contact panels must be narrower than the skin depth, but also the dimension of non-contact panels near the edges and corners of the contact surfaces. This implies that when discretizing long wires, such as in transmission line configurations, many tightly interacting long and thin panels are produced. The problem with these high-aspect-ratio panels is that they worsen the efficiency of clustering-based fast solvers [12, 6, 5].

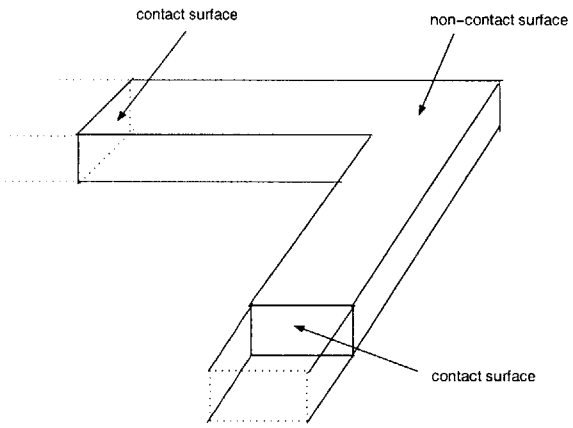

Figure 1-1: A conductor structure

The methodology described in this thesis modifies a crucial area in the surface integral package FastImp. Instead of using piecewise constant basis functions on the contact surfaces of a conductor as implemented in FastImp, our method utilizes a different set of basis functions that captures skin effects in a more efficient and accurate manner. It has been shown that a set of basis functions, generated from

solutions to the Helmholtz equation, can be combined with a standard Galerkin technique to solve a system of "volume-based" Mixed-Potential Integral Equations [2]. This approach has proved to be effective in capturing skin and proximity effects. In this thesis, the basis functions, first seen in a volume-based integral solver, are now adapted into the surface integral solver FastImp. Modifications are made on these basis functions from their original forms in the volume method [2] by confining each basis function to its area of optimal field distribution on a given surface. It has been found that this technique improves the linear independence of the basis functions. In the method presented in this thesis, the new basis functions are only applied on the contact surfaces of the conductor. Piecewise constant basis functions are used on the non-contact surfaces of the conductor. A standard Galerkin technique is applied when field evaluations are made on the contact surfaces while a centroid collocation scheme is used when field evaluations are made on the non-contact surfaces. It will be shown that the use of the Galerkin technique dramatically improves the accuracy of contact current computation and impedance extraction at low frequencies.

In this thesis, we will also show that the exponential field distribution on the contacts can be captured by only a few conduction modes. The implementation of these conduction mode basis functions eliminates not only the constraint of having a fine discretization on the contact surfaces but also on the non-contact surfaces as required in FastImp. In comparison to FastImp, for the same final accuracy, a much coarser discretization is therefore needed, and a much smaller number of tightly interacting panels are then produced. With smaller aspect ratios, these panels are able to take full advantage of the acceleration provided by clustering-based fast solvers such as PFFT.

In short, this thesis offers a unified, more accurate and more cost-effective method of calculating contact current and conductor impedance. It will be shown that this new method addresses the inadequacies of the FastImp algorithm and offers a significant improvement in memory usage and computational speed.

1.4 Overview

This thesis is organized as follows: Chapter 2 presents a description of the system of surface integral formulation. Most of the material in this section is not new research, but is included for the sake of completeness and as a possible source of future reference. Chapter 3 offers a detailed description of the basis functions used. Chapter 4 shows the discretization of the integral equations and the assembly of the system matrix. Chapter 5 presents some of the computational results obtained using the new method. The new method's performance in comparison to FastImp and FastHenry is also discussed.

Chapter 2

Surface integral formulation for full-wave impedance extraction

The surface formulation described in this chapter is developed for the full-wave analysis of time harmonic electromagnetic field. Consider an example of multiple conductors as shown in Figure 2-1.

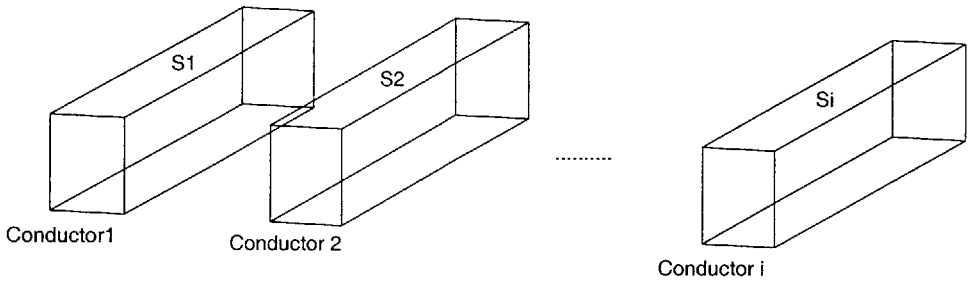

Figure 2-1: A system of conductors

It is assumed that permeability μ and permittivity ε are constant and applicable to the entire problem space while conductivity, σ_i, is constant and applies to individual conductor i. The following Maxwell equations are fundamental laws governing the behavior of the time harmonic electromagnetic fields in the entire problem domain that consists of the conductor media and free space:

$$\nabla \times \overline{E} = -j\omega\mu\overline{H} \tag{2.1}$$

$$\nabla \times \overline{H} = \overline{J} + j\omega\varepsilon\overline{E} \tag{2.2}$$

$$\nabla \cdot (\varepsilon\overline{E}) = \rho \tag{2.3}$$

$$\nabla \cdot (\mu\overline{H}) = 0, \tag{2.4}$$

where E, H:$R^3 \rightarrow R^3$ are the space dependent electric and magnetic fields and J:$R^3 \rightarrow R^3$ is the electric current density.

Each conductor is characterized by Ohm's law which relates conduction current $\overline{J}$ to electric field $\overline{E}$ by conductivity σ_i, where

$$\sigma_i\overline{E} = \overline{J}. \tag{2.5}$$

2.1 First dyadic surface integral equation

The electric field inside of a conductor satisfies a dyadic integral equation that is derived from (2.1) and (2.2). In particular, apply the curl operation to both sides of (2.1), substitute the vector identity $\nabla \times \nabla \times \overline{E} = \nabla(\nabla \cdot \overline{E}) - \nabla^2\overline{E}$ with $\nabla \cdot \overline{E} = 0$ inside of each conductor and the equation $\nabla \times \overline{H} = \sigma\overline{E} + j\omega\varepsilon\overline{E}$, the following vector Helmholtz equation can be derived:

$$(\nabla^2 + \omega^2\mu\varepsilon - j\omega\mu\sigma)\overline{E} = 0. \tag{2.6}$$

Let $k_1 = \sqrt{\omega^2\mu\varepsilon - j\omega\mu\sigma}$, then (2.6) can be expressed as:

$$(\nabla^2 + k_1^2)\overline{E} = 0. \tag{2.7}$$

According to Green's Second Identity[15], the solution to the above wave equation is:

$$\frac{1}{2}\overline{E}(\overline{r}) = \int_{S_i} dS' \left[G_1(\overline{r}, \overline{r'}) \frac{\partial \overline{E}(\overline{r'})}{\partial n(\overline{r'})} - \frac{\partial G_1(\overline{r}, \overline{r'})}{\partial n(\overline{r'})} \overline{E}(\overline{r'}) \right] \tag{2.8}$$

with

$$G_1(\overline{r}, \overline{r'}) = \frac{e^{jk_1|\overline{r} - \overline{r'}|}}{4\pi|\overline{r} - \overline{r'}|}, \tag{2.9}$$

where S_i is the surface of the i-th conductor and G_1 is the scalar Green's function as defined in (2.9). In general, a Green's function enables one to determine the electric

field response at a test point due to a given point source [14]. In (2.8) and (2.9), the location of the test point is specified by position vector $\overline{r}$ and that of the source point is specified by position vector $\overline{r'}$.

According to Green's Second Identity, field solutions inside of a volume is completely determined by the fields on the enclosing surface of the volume. Therefore fields inside of a conductor can be determined by integrating the relation formed by the Green's function over the bounding surface of the conductor as demonstrated in (2.8). In mathematical terms, solution (2.8) expresses the electric field inside of a conductor volume in terms of the electric field and its normal derivative at the conductor surface.

2.2 Second dyadic surface integral equation

The second dyadic surface integral equation applies to the union of all conductors in the problem domain. A macroscopic view is taken by treating the individual conductors as current sources $\overline{J}$ in free space. Thus this equation accounts for the coupling of the electromagnetic fields of the conductors.

A Helmholtz equation is obtained by considering the first two of the Maxwell equations (2.1) and (2.2), yielding:

$$(\nabla^2 + k_0)\overline{E} = j\omega\mu\overline{J}, \tag{2.10}$$

where $k_0 = \omega\sqrt{\varepsilon\mu}$. Green's Second Identity [15] then implies that $\overline{E}$ and $\overline{J}$ satisfy:

$$T\overline{E}(\overline{r}) = \int_{S_i} ds' \left[G_0(\overline{r},\overline{r'}) \frac{\partial \overline{E}(\overline{r'})}{\partial n(\overline{r'})} - \frac{\partial G_0(\overline{r},\overline{r'})}{\partial n(\overline{r'})} \overline{E}(\overline{r'}) \right] + j\omega\mu \int_{V_i} dv' G_0(\overline{r},\overline{r'}) \overline{J}(\overline{r'}), \tag{2.11}$$

where V_i is the volume of the ith conductor, S_i is its surface area and

$$T = \begin{cases} 1 & \text{if } \overline{r} \in V_i \\ \frac{1}{2} & \text{if } \overline{r} \in S_i \\ 0 & \text{otherwise.} \end{cases}$$

The Green's function associated with (2.11) is given by:

$$G_0(\overline{r},\overline{r'}) = \frac{e^{jk_0|\overline{r}-\overline{r'}|}}{4\pi|\overline{r}-\overline{r'}|}. \tag{2.12}$$

Now consider a system of two conductors. If $\overline{r}$ resides on the first conductor surface, then according to (2.11):

$$\frac{1}{2}\overline{E}(\overline{r}) = \int_{S_1} ds' \left[G_0(\overline{r},\overline{r'}) \frac{\partial \overline{E}(\overline{r'})}{\partial n(\overline{r'})} - \frac{\partial G_0(\overline{r},\overline{r'})}{\partial n(\overline{r'})} \overline{E}(\overline{r'}) \right] + j\omega\mu \int_{V_1} dv' G_0(\overline{r},\overline{r'}) \overline{J}(\overline{r'}). \tag{2.13}$$

If $\overline{r}$ is on the first conductor then (2.11) for the second conductor yields:

$$0 = \int_{S_2} ds' \left[G_0(\overline{r},\overline{r'}) \frac{\partial \overline{E}(\overline{r'})}{\partial n(\overline{r'})} - \frac{\partial G_0(\overline{r},\overline{r'})}{\partial n(\overline{r'})} \overline{E}(\overline{r'}) \right] + j\omega\mu \int_{V_2} dv' G_0(\overline{r},\overline{r'}) \overline{J}(\overline{r'}). \tag{2.14}$$

The sum of (2.13) and (2.14) is:

$$\frac{1}{2}\overline{E}(\overline{r}) = \int_{S_1+S_2} ds' \left[G_0(\overline{r},\overline{r'}) \frac{\partial \overline{E}(\overline{r'})}{\partial n(\overline{r'})} - \frac{\partial G_0(\overline{r},\overline{r'})}{\partial n(\overline{r'})} \overline{E}(\overline{r'}) \right] + j\omega\mu \int_{V_1+V_2} dv' G_0(\overline{r},\overline{r'}) \overline{J}(\overline{r'}). \tag{2.15}$$

Consequently, the second dyadic equation can be written in the intergral form:

$$\frac{1}{2}\overline{E}(\overline{r}) = \int_{S} ds' \left[G_0(\overline{r},\overline{r'}) \frac{\partial \overline{E}(\overline{r'})}{\partial n(\overline{r'})} - \frac{\partial G_0(\overline{r},\overline{r'})}{\partial n(\overline{r'})} \overline{E}(\overline{r'}) \right] + j\omega\mu \int_{V} dv' G_0(\overline{r},\overline{r'}) \overline{J}(\overline{r'}), \tag{2.16}$$

where V is the union of all conductor volumes and S is the union of all conductor surfaces.

The volume integral in (2.16) can be expressed in a non-integral form by considering the following equation:

$$j\omega\overline{A}(\overline{r}) = \nabla\phi(\overline{r}) + \overline{E}(\overline{r}), \tag{2.17}$$

where $\overline{A}$ is the magnetic vector potential and ϕ is the scalar electric potential. According to [16], the magnetic vector potential $\overline{A}(\overline{r})$ is defined as:

$$\overline{A}(\overline{r}) = \int_{V} G_0(\overline{r},\overline{r'}) \mu \overline{J}(\overline{r'}). \tag{2.18}$$

Therefore, (2.17) becomes:

$$j\omega\mu \int_{V} dv' G_0(\overline{r},\overline{r'}) \overline{J}(\overline{r'}) = \nabla\phi(\overline{r}) + \overline{E}(\overline{r}), \tag{2.19}$$

The second dyadic surface integral equation can then be written in the surface integral form:

$$-\frac{1}{2}\overline{E}(\overline{r}) = \int_{S} ds' \left[G_0(\overline{r},\overline{r'}) \frac{\partial \overline{E}(\overline{r'})}{\partial n(\overline{r'})} - \frac{\partial G_0(\overline{r},\overline{r'})}{\partial n(\overline{r'})} \overline{E}(\overline{r'}) \right] + \nabla\phi(\overline{r}), \tag{2.20}$$

where S is the union of all conductor surfaces. Intuitively, one can see that this equation relates the gradient of the scalar electric potential to the electric field and its normal derivative on the surface of all conductors.

2.3 Scalar Poisson surface integral equation

According to the well known "mixed-potential" formulation, Maxwell differential equations (2.1)-(2.4) can be expressed in the form of an electric scalar potential ϕ satisfying:

$$(\nabla^2 + k_0^2)\phi = \frac{\rho}{\varepsilon}, \tag{2.21}$$

where $K_0 = \omega\sqrt{\varepsilon\mu}$. In a surface integral form, (2.21) is written as:

$$\phi(\overline{r}) = \int_S dS' G_0(\overline{r}, \overline{r'}) \frac{\rho(\overline{r'})}{\varepsilon}, \tag{2.22}$$

where G_0 is the same as the Green's function defined in (2.12).

2.4 Expression of current conservation as a surface integral equation

$\nabla \cdot \overline{E} = 0$ holds true inside of a conductor volume [14]. A surface form of this equation must be derived. This can be accomplished by considering a volume V shaped like a rectangular pillbox as illustrated in Figure 2-2. The top and bottom surfaces of the box have area a and closed contour C and are situated such that the top face is on the conductor surface while the bottom face is a distance δ beneath the surface.

Current conservation can be accounted for by noting that the current flows from the top, bottom and sides of the box adds up to zero [16], that is,

$$\int_c dc\,[\delta E_t \cdot (n(\overline{r}) \times \ell(\overline{r}))] - \int_{a_1}^{b_1}\int_{a_2}^{b_2} dt_1 dt_2\,[E_n(t_1, t_2, 0) - E_n(t_1, t_2, -\delta)] = 0. \tag{2.23}$$

The line integral along contour C in (2.23) accounts for contributions of current tangential to the pillbox, that is, entering from the sides. In this integral, n is the

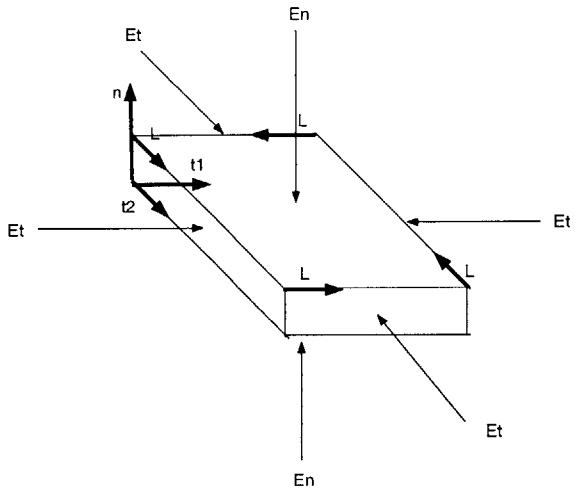

Figure 2-2: A sample surface for current conservation

unit normal vector of the top or bottom face while ℓ is the unit vector along contour C, and $n \times \ell$ indicates the tangential direction of current flow.

The area integral in the second term of (2.23) accounts for the contributions of current entering the box from the normal directions, that is, from top and bottom of the box. In this integral, a local coordinate system (t_1, t_2, n) is used. The two mutually orthogonal unit vectors t_1 and t_2 indicate the tangential location of a point within a plane surface while unit vector n indicates the normal placement of this point in relation to the plane surface. Therefore $(t_1, t_2, 0)$ and $(t_1, t_2, -\delta)$ describe any point that is located on the top and bottom faces of the box, respectively.

In (2.23), let δ approach zero in the integrand of the line integral and apply Taylor expansion to the integrand of the area integral. The following surface integral form of current conservation is then obtained:

$$\int_c dc\,[E_t(\overline{r}) \cdot (n(\overline{r}) \times \ell(\overline{r}))] - \int_a da \frac{\partial E_n(\overline{r})}{\partial n(\overline{r})} = 0. \tag{2.24}$$

2.5 Boundary conditions

In the case of general full-wave impedance extractions, normal boundary conditions for the non-contact conductor surface can be derived by considering the charge con-

servation law

$$\nabla \cdot \overline{J}(\overline{r}) = -j\omega\rho(\overline{r}). \tag{2.25}$$

From (2.25), one sees that the surface normal boundary condition on the non-contact surfaces is:

$$E_n(\overline{r}) = \frac{j\omega\rho(\overline{r})}{\sigma}. \tag{2.26}$$

A different set of boundary conditions exists for the contact surfaces of a conductor to which the terminals are attached. We assume that a constant input current is applied to each terminal in the surface normal direction. Then the electrical field along the tangential directions of the contact can be assumed to be zero. In addition, since the applied current is constant, changes of the electrical field along the normal direction of the contact can also be assumed to be zero, that is, $\frac{\partial E_n}{\partial n} = 0$. Moreover, it can be assumed that changes of the tangential electrical fields along the normal direction are negligible, that is, $\frac{\partial E_{t_1}}{\partial n} = 0$ and $\frac{\partial E_{t_2}}{\partial n} = 0$. In mathematical terms, the boundary conditions on each contact surface are summarized as:

$$\overline{E}(\overline{r}) = \hat{n}E_n(\overline{r}), \quad \overline{r} \in S_c \tag{2.27}$$

and

$$\frac{\partial \overline{E}(\overline{r})}{\partial n} = 0, \quad \overline{r} \in S_c, \tag{2.28}$$

where S_c denotes the contact surfaces of a conductor and $\hat{n}$ is the outward surface normal unit vector.

Finally, since voltages are applied to the contact terminals, electric potentials on the contacts are known. They are either positive or negative constants depending on the polarity of the terminals, that is:

$$\phi(\overline{r}) = c. \tag{2.29}$$

2.6 Surface integral formulation summary

To summarize, the surface integral formulation consists of four surface integral equations and several boundary conditions:

1. The first dyadic surface integral equation:

$$\frac{1}{2}\overline{E}(\overline{r}) = \int_{S_i} dS' \left[G_1(\overline{r},\overline{r'}) \frac{\partial \overline{E}(\overline{r'})}{\partial n(\overline{r'})} - \frac{\partial G_1(\overline{r},\overline{r'})}{\partial n(\overline{r'})} \overline{E}(\overline{r'}) \right]$$
$$G_1(\overline{r},\overline{r'}) = \frac{e^{jk_1|\overline{r}-\overline{r'}|}}{4\pi|\overline{r}-\overline{r'}|}, k_1 = \sqrt{\omega^2\mu\varepsilon - j\omega\mu\sigma},$$

where S_i is the surface of the ith conductor.

2. The second dyadic surface integral equation:

$$-\frac{1}{2}\overline{E}(\overline{r}) = \int_S ds' \left[G_0(\overline{r},\overline{r'}) \frac{\partial \overline{E}(\overline{r'})}{\partial n(\overline{r'})} - \frac{\partial G_0(\overline{r},\overline{r'})}{\partial n(\overline{r'})} \overline{E}(\overline{r'}) \right] + \nabla\phi(\overline{r})$$
$$G_0(\overline{r},\overline{r'}) = \frac{e^{jk_0|\overline{r}-\overline{r'}|}}{4\pi|\overline{r}-\overline{r'}|}, k_0 = \omega\sqrt{\varepsilon\mu},$$

where S is the union of all conductor surfaces.

3. The surface potential integral equation:

$$\phi(\overline{r}) = \int_{s_i'} ds' G_0(\overline{r},\overline{r'}) \frac{\rho(\overline{r'})}{\varepsilon}$$
$$G_0(\overline{r},\overline{r'}) = \frac{e^{jk_0|\overline{r}-\overline{r'}|}}{4\pi|\overline{r}-\overline{r'}|}, k_0 = \omega\sqrt{\varepsilon\mu}.$$

4. The surface integral form of current conservation:

$$\int_c dc \left[E_t(\overline{r}) \cdot (n(\overline{r}) \times \ell(\overline{r})) \right] - \int_a da \frac{\partial E_n(\overline{r})}{\partial n(\overline{r})} = 0.$$

5. Boundary conditions for non-contact surface:

$$E_n(\overline{r}) = \frac{j\omega\rho(\overline{r})}{\sigma}.$$

6. Boundary conditions for contacts:

$$\overline{E}(\overline{r}) = \hat{n} E_n(\overline{r})$$
$$\frac{\partial \overline{E}(\overline{r})}{\partial n} = 0$$
$$\phi(\overline{r}) = c.$$

Under the global coordinate system of (x, y, z), there exists eight unknowns, grouped into four categories, that are associated with the above full-wave formulation. They are: the electric field components E_x, E_y and E_z, the components of the surface normal derivative of the electric field $\frac{\partial E_x}{\partial n}$, $\frac{\partial E_y}{\partial n}$, and $\frac{\partial E_z}{\partial n}$, the scalar surface charge density ρ, and the scalar electric potential ϕ.

2.7 Impedance extraction

For a conductor operating at a certain frequency f with a potential difference $\phi_A - \phi_B = V_{diff}$ applied between its two terminals A and B, a system of integral equations can be formed utilizing the above formulation. The normal electric field on a contact, E_n, is then obtained by solving the system. Subsequently, E_n is used to compute contact current utilizing the equation:

$$\overline{I}(\overline{r}) = \hat{n}\sigma \int_{S_c} dr E_n(\overline{r}). \tag{2.30}$$

Once the contact current is known, the impedance of the conductor at each frequency level is calculated as:

$$Z = \frac{V_{diff}}{I}. \tag{2.31}$$

Resistance R, inductance L, and capacitance C are defined as:

$$R = Re\{Z\} \tag{2.32}$$

and

$$L = \frac{Im\{Z\}}{2\pi f} \qquad if Im\{Z\} > 0 \tag{2.33}$$

$$C = \frac{1}{Im\{Z\} \times 2\pi f} \quad if Im\{Z\} < 0. \tag{2.34}$$

Chapter 3

Basis functions for each type of unknowns

In this chapter, it will be shown that each type of unknowns, $\overline{E}$, $\frac{\partial \overline{E}}{\partial n}$, ρ and ϕ, can be approximated by a weighted sum of basis functions. In turn, the conductor surface must be discretized in manners so as to support the basis functions associated with each type of unknowns. In the case of non-contact surfaces, consider representing $\overline{E}$, $\frac{\partial \overline{E}}{\partial n}$, ρ and ϕ using piecewise constant basis functions; therefore the non-contact surfaces are discretized into N^{NC} regular quadrilateral panels consisting of M^{NC} vertices. In the case of contact surfaces, consider using piecewise constant basis functions to present ρ and ϕ; therefore the contact surfaces are discretized into N^{C} quadrilateral panels with M^{C} vertices. Consider using a set of conduction mode basis functions to represent $\overline{E}$ on each contact surface; since each contact is considered to be a basis of support for the set of conduction modes, no contact surface discretization is need. Finally, it should be noted that $\frac{\partial \overline{E}}{\partial n}$ is negligible on the contact surface according to boundary condition (2.28).

3.1 Electric field

3.1.1 Conduction mode basis functions on contact surfaces

Background

Input contact current and conductor impedance can only be accurately determined if the electric field on the contact is accurately represented. However, it becomes more difficult to calculate the electric field on the contact as operating frequencies increase. This is because current at high frequencies crowd near the edges and corners of the contact's cross-sectional surface, thus generating skin effects. One dimensional analysis [17] shows that inside a conductor, the current density decays exponentially with distance from the conductor surface. The decay rate increases as operating frequency increases. Customarily, more refined discretization of the contact surface is needed to capture the crowding of the fields on the contact edges and corners. To avoid such computationally expensive endeavor, one can take advantage of the knowledge of this exponential decay to model the field distribution on the contact.

A volume integral formulation that has successfully modeled the skin and proximity effects of a conductor at high frequencies is presented in [2]. First consider equation (2.6) for the region inside of a conductor. Assuming that $\sigma \gg j\omega\varepsilon$ in a "good" conductor, the governing Helmholtz diffusion equation for each contact surface of the conductor is obtained to be:

$$[\nabla^2 - (\frac{1+j}{\delta})]\overline{E} = 0, \tag{3.1}$$

where $\delta = \sqrt{\frac{2}{\omega\mu\sigma}}$ is the skin depth. According to boundary condition (2.27), it is assumed that the electric field on a contact exists only in the surface normal direction. Equation (3.1) thus yields:

$$\frac{\partial^2 E_n}{\partial t_1^2} + \frac{\partial^2 E_n}{\partial t_2^2} - (\frac{1+j}{\delta})E_n = 0, \tag{3.2}$$

where t_1 and t_2 are two mutually orthogonal tangential unit vectors of the contact. The general solutions to (3.2) are the infinite series:

$$E_n(t_1, t_2) = \sum_k C_k e^{-a_k t_1} e^{-b_k t_2}, \tag{3.3}$$

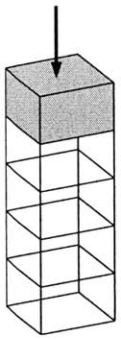

Figure 3-1: Volume discretization of a conductor with each section supporting a set of conduction mode basis functions. The arrow indicates the direction of current flow.

where n denotes the surface normal of the contact surface. Coordinate system (t_1, t_2) is used to specify any point in the plane of the contact. C_k's are scalar coefficients. Exponents a_k and b_k satisfy the following constraint:

$$a_k^2 + b_k^2 = \left(\frac{1+j}{\delta}\right)^2. \tag{3.4}$$

Each term in the infinite series (3.3) represents a "conduction mode."

As presented in [2], in order to model conductor current flow using a volume-based method, a conductor is subdivided along its length into sections that are short compare to the smallest wavelength. A set of conduction mode basis functions is applied to each section. An example of this discretization is shown in Figure 3-1.

Using conduction modes in the surface integral formulation FastImp

A major observation of our research is that the volume-based conduction mode basis functions can be modified to be used in a surface formulation so as to accurately and efficiently model contact surface current flow. For the volume-based method, a set of conduction mode basis functions is applied to each subdivided segment volume as shown in Figure 3-1. On the other hand, for the surface-based method, the conduction mode basis functions are only applied on each conductor contact surface, thereby reducing the number of unknowns in comparison to the volume-based method, especially as the number of conductor volume subdivisions increase with the increase of operating frequencies.

The normal electric field distributions on a contact, E_n, can be accurately represented by just a few of the infinitely many conduction modes. Specifically, we use eight such modes. Four modes are "side modes" and they capture the field exponentially decaying from each side of a conductor contact cross section. The combination of all four side modes is able to account for most of the high frequency conductor field distribution on a contact. At extremely high frequencies, four additional "corner" modes are necessary to account for the extra distributions decaying from the four corners of the contact. A side mode is specified by letting

$$a_s = \frac{1+j}{\delta} \quad and \quad b_s = 0. \tag{3.5}$$

A corner mode is specified by letting

$$a_s = \frac{1}{\sqrt{2}}(\frac{1+j}{\delta}) \quad and \quad b_s = \frac{1}{\sqrt{2}}(\frac{1+j}{\delta}). \tag{3.6}$$

However, if each one of the eight conduction modes were implemented over the entire area of the contact surface, numerical difficulties would arise at low frequencies due to the fact that the relative flatness of the contact electric field at low frequencies makes all the conduction modes resemble each other. This lack of distinctions between modes introduces linear dependency between the system of discretized integral equations at low frequencies. The system thus becomes ill-conditioned and solving it using an iterative method would require many iterations. This problem can be rectified by confining conduction modes to areas on the contact that reduces the amount of overlaps between modes while maintaining their effectiveness. For instance, the coverage of each mode can be reduced to a half or a quarter of the contact area. Therefore the four side modes are confined to the left half, right half, top half and bottom half of the contact. The four corner modes are confined to the upper left quarter, lower left quarter, upper right quarter and lower right quarter of the contact.

Figure 3-2 and Figure 3-3 show the shapes of one truncated side mode and one truncated corner mode, respectively. As demonstrated, the truncated side conduction mode only contributes to the electric field distribution on one half of the contact plane while the truncated corner mode only contributes to one quarter of the entire contact electric field distribution.

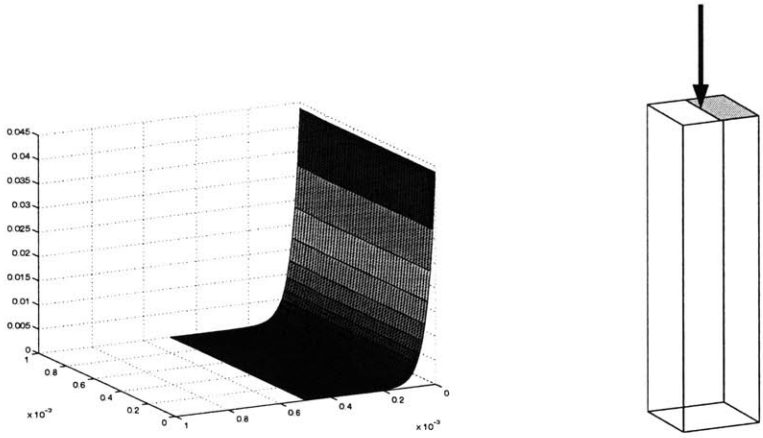

Figure 3-2: A side mode contact surface electric field distribution and its optimal contact area coverage. The arrow indicates the direction of current flow.

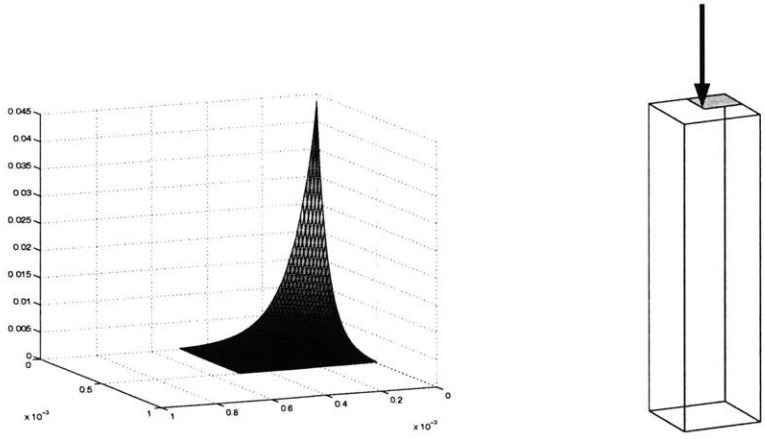

Figure 3-3: A corner mode contact surface electric field distribution and its optimal contact area coverage.

In general, the electric field on a contact can be written as a weighted sum of field contributions from all eight truncated conduction modes. That is:

$$\overline{E}_{S_c}(\overline{r}) = \hat{n}_c \sum_{j=1}^{N^M} C_j W_j(\overline{r}), \tag{3.7}$$

where W_j denotes the jth conduction mode basis function, and N^M is the total number of conduction mode basis functions used on each contact. Figure 3-4 shows an example of contact electric field representation using all eight conduction mode basis functions, that is, four truncated side modes and four truncated corner modes.

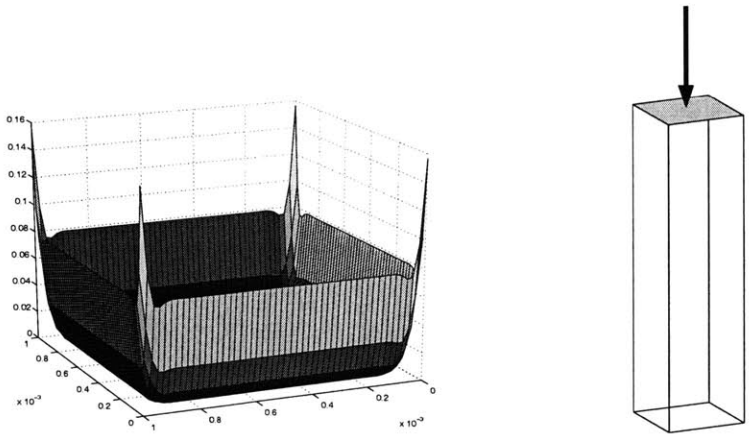

Figure 3-4: Electric field representation using all eight truncated conduction mode basis functions on a contact.

3.1.2 Piecewise constant basis functions on non-contact surfaces

Non-contact conductor surfaces are discretized into N^{NC} quadrilateral panels with the assumption that the electric field is constant on each panel. It should be noted that the global coordinate system of (x, y, z) is used when dealing with fields on the non-contact surfaces. Therefore the electric field associated with each panel is decomposed into E_x, E_y and E_z components. The electric field on the non-contact surfaces can thus be expressed as a sum of combined contributions from the directional

components on all the non-contact panels. That is,

$$\overline{E}_{S_{nc}}(\overline{r}) = \sum_{j=1}^{N^{NC}} (\hat{x}E_{x_j} + \hat{y}E_{y_j} + \hat{z}E_{z_j})P_{cj}(\overline{r}), \tag{3.8}$$

where P_{cj} is a piecewise constant function defined as:

$$P_{cj}(\overline{r}) = \begin{cases} 1 & \text{if } \overline{r} \in Panel_j \\ 0 & \text{otherwise} \end{cases}.$$

3.1.3 Basis functions on the entire conductor surface

The electric field on the entire conductor surface can be represented as a sum of electric field on the contact surfaces (S_c) and on the non-contact surfaces (S_{nc}) of the conductor. That is,

$$\overline{E}(\overline{r}) = \overline{E}_{S_c}(\overline{r}) + \overline{E}_{S_{nc}}(\overline{r}). \tag{3.9}$$

Substituting (3.7) and (3.8) into (3.9) yields:

$$\overline{E}(\overline{r}) = \hat{n}_c \sum_{j=1}^{N^M} C_j W_j(\overline{r}) + \sum_{j=1}^{N^{NC}} (\hat{x}E_{x_j} + \hat{y}E_{y_j} + \hat{z}E_{z_j})P_{cj}(\overline{r}). \tag{3.10}$$

Figure 3-5 shows the overall conductor surface discretization required to support the basis function representations of the electric field on the contact and non-contact surfaces.

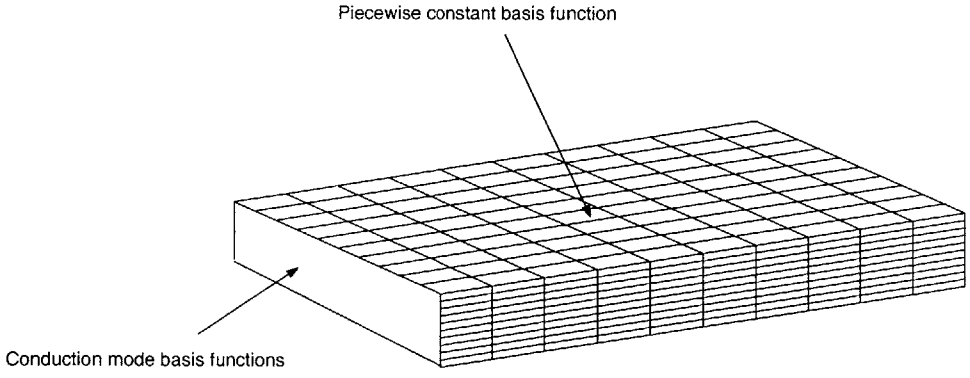

Figure 3-5: Conductor surface discretization for the electric field $\overline{E}$.

3.2 Surface normal derivative of the electric field

According to (2.28), the surface normal derivative of the electric field is negligible on the contacts. Therefore,

$$\frac{\partial \overline{E}(\overline{r})}{\partial n} = \frac{\partial \overline{E}_{S_{nc}}(\overline{r})}{\partial n}. \tag{3.11}$$

The non-contact conductor surface is dicretized into N^{NC} panels with the assumption that $\frac{\partial \overline{E}}{\partial n}$ is constant on each panel. Using the piece-wise constant basis function representation, $\frac{\partial \overline{E}}{\partial n}$ over the entire non-contact surface can be expressed as a sum of $\frac{\partial \overline{E}}{\partial n}$ on all the non-contact panels. That is,

$$\frac{\partial \overline{E}(\overline{r})}{\partial n} = \sum_{j=1}^{N^{NC}} (\hat{x}\frac{\partial E_{x_j}}{\partial n} + \hat{y}\frac{\partial E_{y_j}}{\partial n} + \hat{z}\frac{\partial E_{z_j}}{\partial n}) P_{cj}(\overline{r}). \tag{3.12}$$

3.3 Surface charge density and electric potential

Surface charge density ρ is approximated by discretizing the entire conductor surface into N quadrilateral panels. Assuming that ρ is constant on each discretized panel, then the sum of ρ on all the panels would approximate the charge density on the entire conductor surface. That is,

$$\rho(\overline{r}) = \sum_{j=1}^{N} \rho_j P_{cj}(\overline{r}). \tag{3.13}$$

Similarly, conductor electric potential ϕ is represented as a sum of panel potentials over the entire conductor surface:

$$\phi(\overline{r}) = \sum_{j=1}^{N} \phi_j P_{cj}(\overline{r}). \tag{3.14}$$

Furthermore, in an effort to relate each panel centroid potential to the potentials at panel vertices, one can assume that the potentials at the four vertices contribute equally to the potential at the centroid of the panel. That is:

$$\phi_j = \sum_{k=1}^{4} \frac{1}{4}\phi(v_{jk}), \tag{3.15}$$

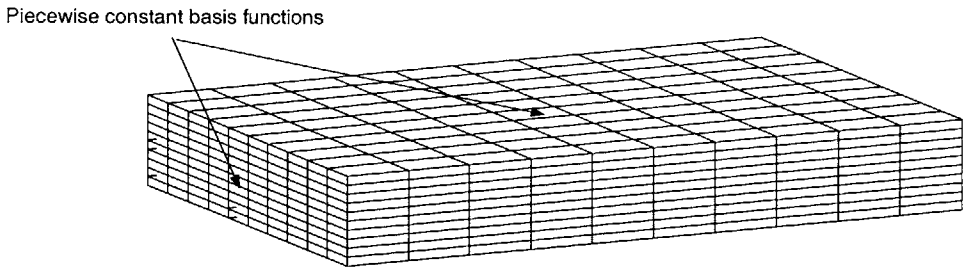

Figure 3-6: Conductor surface discretization for ϕ, ρ and $\frac{\partial \overline{E}}{\partial n}$.

where v_{jk} is the kth vertex of panel j. Substitute (3.15) into (3.14) for ϕ yields the piece-wise constant basis function representation of the electric potential:

$$\phi(\overline{r}) = \sum_{j=1}^{N} \sum_{k=1}^{4} \frac{1}{4} \phi(v_{jk}) P_{cj}(\overline{r}). \tag{3.16}$$

Figure 3-6 shows the overall conductor surface discretization required to support the basis functions of ϕ, ρ and $\frac{\partial \overline{E}}{\partial n}$. It is worth mentioning at this point that only the non-contact conductor surface discretization is used to support the basis functions of $\frac{\partial \overline{E}}{\partial n}$.

3.4 Basis functions summary

1. For the electric field:

$$\overline{E}(\overline{r}) = \hat{n}_c \sum_{j=1}^{N^M} C_j W_j(\overline{r}) + \sum_{j=1}^{N^{NC}} (\hat{x} E_{x_j} + \hat{y} E_{y_j} + \hat{z} E_{z_j}) P_{cj}(\overline{r}).$$

2. For the surface normal derivative of the electric field:

$$\frac{\partial \overline{E}(\overline{r})}{\partial n} = \sum_{j=1}^{N^{NC}} (\hat{x} \frac{\partial E_{x_j}}{\partial n} + \hat{y} \frac{\partial E_{y_j}}{\partial n} + \hat{z} \frac{\partial E_{z_j}}{\partial n}) P_{cj}(\overline{r}).$$

3. For the charge density:

$$\rho(\overline{r}) = \sum_{j=1}^{N} \rho_j P_{cj}(\overline{r}).$$

4. For the electric potential:

$$\phi(\overline{r}) = \sum_{j=1}^{N} \sum_{k=1}^{4} \tfrac{1}{4} \phi(v_{jk}) P_{cj}(\overline{r}).$$

Chapter 4

Discretization

In Chapter 3, the basis functions for each type of unknowns have been defined along with the surface discretization required to support those basis functions. In this chapter, a mix of standard Galerkin and centroid collocation techniques is used to generate a system of discretized equations for the weights of the basis functions. In turn, these weights can be utilized to compute terminal current and extract conductor impedance.

4.1 Discretization of the first dyadic surface integral equation

The first dyadic surface integral equation given by (2.8) can be written explicitly as a sum of integrals over non-contact and contact conductor surfaces:

$$\int_{S_{nc}} ds' G_1(\overline{r}, \overline{r'}) \frac{\partial \overline{E}(\overline{r})}{\partial n} - (\int_{S_{nc}} + \int_{S_c}) ds' \frac{\partial G_1(\overline{r}, \overline{r'})}{\partial n} \overline{E}(\overline{r}) - \frac{1}{2} \overline{E}(\overline{r}) = 0, \tag{4.1}$$

where S_{nc} denotes the non-contact surfaces and S_c denotes the contact surfaces. Since $\frac{\partial \overline{E}}{\partial n}$ is assumed to be negligible on the contacts according to boundary condition (2.28), then only the non-contact surface integral of $\frac{\partial \overline{E}}{\partial n}$ is applied to (4.1).

Let $\overline{f_1}(\overline{r})$ equal to the first term of (4.1), that is,

$$\overline{f_1}(\overline{r}) = \int_{S_{nc}} ds' G_1(\overline{r}, \overline{r'}) \frac{\partial \overline{E}(\overline{r})}{\partial n}. \tag{4.2}$$

Substituting basis function (3.12) for $\frac{\partial \overline{E}}{\partial n}$ in (4.2) yields the expanded integral:

$$\overline{f_1}(\overline{r}) = \sum_{j=1}^{N^{NC}} (\hat{x}\frac{\partial E_{x_j}}{\partial n} + \hat{y}\frac{\partial E_{y_j}}{\partial n} + \hat{z}\frac{\partial E_{z_j}}{\partial n}) \int_{S_{nc_j}} ds' G_1(\overline{r}, \overline{r'}), \tag{4.3}$$

where S_{nc_j} is the surface of the jth non-contact panel.

Let $\overline{f_2}(\overline{r})$ equal to the second integral term in (4.1), that is,

$$\overline{f_2}(\overline{r}) = -\int_{S_{nc}} ds' \frac{\partial G_1(\overline{r}, \overline{r'})}{\partial n} \overline{E}(\overline{r}). \tag{4.4}$$

Basis function(3.10) defined on the non-contact surfaces is substituted for $\overline{E}$ in (4.4) to yield the following expression:

$$\overline{f_2}(\overline{r}) = -\sum_{j=1}^{N^{NC}} (\hat{x}E_{x_j} + \hat{y}E_{y_j} + \hat{z}E_{z_j}) \int_{S_{nc_j}} ds' \frac{\partial G_1(\overline{r}, \overline{r'})}{\partial n(\overline{r'})}. \tag{4.5}$$

Let $\overline{f_3}(\overline{r})$ be to the third integral term in (4.1), that is,

$$\overline{f_3}(\overline{r}) = -\int_{S_c} ds' \frac{\partial G_1(\overline{r}, \overline{r'})}{\partial n} \overline{E}(\overline{r}). \tag{4.6}$$

Assume that the conductor is a two-ported system, then (4.6) can be decomposed into a left and a right contact surface integral. Using the basis function representation of the contact electric field in (3.7), (4.6) can then be expressed as:

$$\overline{f}_{3_1}(\overline{r}) = -\hat{n_l} \sum_{j=1}^{N^M} C_{l_j} \int_{S_{cl}} ds' \frac{\partial G_1(\overline{r}, \overline{r'})}{\partial n(\overline{r'})} W_j(\overline{r'}) \tag{4.7}$$

and

$$\overline{f}_{3_2}(\overline{r}) = -\hat{n_r} \sum_{j}^{N^M} C_{r_j} \int_{S_{cr}} ds' \frac{\partial G_1(\overline{r}, \overline{r'})}{\partial n(\overline{r'})} W_j(\overline{r'}), \tag{4.8}$$

where S_{cl} and S_{cr} are the left and right contact surfaces, $\hat{n_l}$ and $\hat{n_r}$ are the left and right contact normals, and C_l and C_r are the conduction mode weights of the basis functions representing left and right contact electric fields.

Finally, let $\overline{f_4}(\overline{r})$ equal to the fourth non-integral term in (4.1). Then

$$\overline{f_4}(\overline{r}) = -\frac{1}{2}\overline{E}(\overline{r}). \tag{4.9}$$

Utilizing the basis function representation for the overall electric field in (3.10), (4.9) can be rewritten in the form of:

$$\overline{f_4}(\overline{r}) = -\frac{1}{2}\sum_{j=1}^{N^{NC}} (\hat{x}E_{x_j} + \hat{y}E_{y_j} + \hat{z}E_{z_j}) P_{c_j}(\overline{r}) - \frac{1}{2}\hat{n_l}\sum_{j=1}^{N^M} C_{l_j} W_j(\overline{r}) - \frac{1}{2}\hat{n_r}\sum_{j=1}^{N^M} C_{r_j} W_j(\overline{r}). \tag{4.10}$$

Based on the above expansions, (4.1) can then be represented as a sum of those expanded terms as defined in (4.3), (4.5),(4.7), (4.8) and (4.10), that is:

$$\overline{f_1}(\overline{r}) + \overline{f_2}(\overline{r}) + \overline{f}_{3_1}(\overline{r}) + \overline{f}_{3_2}(\overline{r}) + \overline{f_4}(\overline{r}) = 0. \tag{4.11}$$

A mix of standard Galerkin and centroid collocation techniques is applied to (4.11) to generate a system of equations for the weights, $\frac{\partial E_x}{\partial n}$, $\frac{\partial E_y}{\partial n}$, $\frac{\partial E_z}{\partial n}$, E_x,E_y, E_z, C_l and C_r. The standard Galerkin technique [18] is applied when the electric field evaluations are made on the contact surfaces of a conductor. This Galerkin technique is necessary due to the nature of the conduction mode basis functions, that is, they are non-constant, fast-varying, and need a large area of support (either one half or a quarter of the contact area). In comparison to the Galerkin technique, a more efficient, but less accurate scheme of centroid collocation is applied to the field evaluations made on the non-contact surfaces.

The result is a matrix equation of the form:

$$[A] \begin{bmatrix} \frac{\partial E_x}{\partial n} \\ \frac{\partial E_y}{\partial n} \\ \frac{\partial E_z}{\partial n} \\ E_x \\ E_y \\ E_z \\ C_l \\ C_r \end{bmatrix} = \begin{bmatrix} 0 \\ 0 \\ 0 \\ 0 \\ 0 \end{bmatrix},$$

with A=

$$\begin{bmatrix} P & 0 & 0 & D & 0 & 0 & n_{l_x} L_l & n_{r_x} L_r \\ 0 & P & 0 & 0 & D & 0 & n_{l_y} L_l & n_{r_y} L_r \\ 0 & 0 & P & 0 & 0 & D & n_{l_z} L_l & n_{r_z} L_r \\ n_{l_x} J_l & n_{l_y} J_l & n_{l_z} J_l & n_{l_x} k_l & n_{l_y} k_l & n_{l_z} k_l & D_{ll} & (\hat{n_l} \cdot \hat{n_r}) D_{lr} \\ n_{r_x} J_r & n_{r_y} J_r & n_{r_z} J_r & n_{r_x} k_r & n_{r_y} k_r & n_{r_z} k_r & (\hat{n_r} \cdot \hat{n_l}) D_{rl} & D_{rr} \end{bmatrix},$$

where n_{ℓ_x}, n_{ℓ_y} and n_{ℓ_z} are the projections of the unit normal vector of the left contact onto the global x, y and z coordinates. The same projections are performed on the

unit normal vector of the right contact to produce n_{r_x}, n_{r_y} and n_{r_z}. Derivations for the entries of the submatrices in matrix A will be shown in the next few sections.

The unknown vectors $\frac{\partial E_x}{\partial n}$, $\frac{\partial E_y}{\partial n}$ and $\frac{\partial E_z}{\partial n}$ are the weights of the piecewise-constant basis functions for the normal derivative of the electric field on the non-contact panels. Vectors E_x, E_y and E_z are the weights of the piecewise-constant basis functions for the electric field on the non-contact panels. Vectors C_l and C_r contain the weights of the conduction mode basis functions used to represent the electric field on the left and right contacts, respectively.

The first three rows of matrix A correspond to evaluations made on the non-contact conductor surfaces. Recall from Chapter 3 that the x, y and z field components on the non-contact surfaces are approximated by piecewise constant basis functions. Therefore each row in A is an extraction of a non-contact surface directional field component, x, y or z. A panel centroid collocation scheme is used to produce the submatrix entries in the first three rows of A:

$$P_{ij} = \int_{S_{nc_j}} dr' G_1(\overline{r_{ic}}, \overline{r'}) \tag{4.12}$$

$$D_{ij} = \begin{cases} \int_{S_{nc_j}} dr' \frac{1}{2} & \text{if i=j} \\ -\int_{S_{nc_j}} dr' \frac{\partial G_1(\overline{r}_{ic}, \overline{r'})}{\partial n(\overline{r'})} & \text{if i} \neq \text{j} \end{cases}$$

$$L_{l_{ij}} = -\int_{S_{cl}} dr' \frac{\partial G_1(\overline{r}_{ic}, \overline{r'})}{\partial n(\overline{r'})} W_j(\overline{r'}) \tag{4.13}$$

$$L_{r_{ij}} = -\int_{S_{cr}} dr' \frac{\partial G_1(\overline{r}_{ic}, \overline{r'})}{\partial n(\overline{r'})} W_j(\overline{r'}). \tag{4.14}$$

In (4.12)-(4.14), $\overline{r}_{ic}$ is the centroid of the ith non-contact evaluation panel. Matrices P and D contain $\overline{E}$ and $\frac{\partial \overline{E}}{\partial n}$ field responses, respectively, measured at the centroid of each evaluation panel due to source distribution on each non-contact panel. Matrices J_l and J_r contain the electric field responses measured at the centroid of each evaluation panel due to source distributions on the left contact surface, S_{cl}, and right contact surface, S_{cr}, respectively. Matrices P and D are N^{NC} by N^{NC}, where N^{NC} is the number of non-contact panels. Matrices L_l and L_r are N^{NC} by N^M, where N^M is the number of conduction mode basis functions on each contact.

The last two rows of matrix A correspond to field evaluations made on the contact surfaces. Since only the surface normal component of the electric field is present on the contacts, the last two rows of A contain the extracted normal electric field components on the left and right contacts, respectively. A standard Galerkin technique is used to produce the matrices in the last two rows of matrix A. Using the left contact as an example, the following matrices are produced:

$$J_{l_{ij}} = \int_{S_{cl}} \int_{S_{nc_j}} dr' dr G_1(\overline{r}, \overline{r'}) W_i(\overline{r}) \tag{4.15}$$

$$K_{l_{ij}} = -\int_{S_{cl}} \int_{S_{nc_j}} dr' dr \frac{\partial G_1(\overline{r}, \overline{r'})}{\partial n(\overline{r'})} W_i(\overline{r}) \tag{4.16}$$

$$D_{ll_{ij}} = \frac{1}{2} C_{l_j} \int_{S_{cl}} dr W_i(\overline{r}) W_j(\overline{r}) \tag{4.17}$$

$$D_{lr_{ij}} = -\int_{S_{cl}} \int_{S_{cr}} dr' dr \frac{\partial G_1(\overline{r}, \overline{r'})}{\partial n(\overline{r'})} W_j(\overline{r'}) W_i(\overline{r}). \tag{4.18}$$

Matrices J and K contain the distributed $\overline{E}$ and $\frac{\partial \overline{E}}{\partial n}$ field responses, respectively, over the entire surface of the left contact due to source distribution from each non-contact panel. Matrices D_{ll} and D_{lr} contain the distributed E field responses on the left contact due to source distributions on the left and right contacts, respectively. Similar matrices J_r, K_r, D_{rr} and D_{rl} can be obtained when the field evaluations are made on the right contact surface. Matrices J_l, J_r, K_l and K_r are all N^M by N^{NC}. Matrices D_{ll}, D_{lr}, D_{rl} and D_{rr} are all N^M by N^M.

4.2 Discretization of the second dyadic surface integral equation

The second dyadic equation given by (2.20) can be written as a sum of contact and non-contact surface integrals:

$$\int_{S_{nc}} ds' G_0(\overline{r}, \overline{r'}) \frac{\partial \overline{E}(\overline{r})}{\partial n} - (\int_{S_{nc}} + \int_{S_c}) ds' \frac{\partial G_0(\overline{r}, \overline{r'})}{\partial n} \overline{E}(\overline{r}) + \frac{1}{2} \overline{E}(\overline{r}) + \nabla \phi(\overline{r}) = 0. \tag{4.19}$$

Equation (4.19) is similar to (4.1) with the exception of the $\nabla\phi$ term that is defined as:

$$\nabla \phi(\overline{r}) = \hat{t_1} \frac{\partial \phi}{\partial t_1} + \hat{t_2} \frac{\partial \phi}{\partial t_2} + \hat{n} \frac{\partial \phi}{\partial n}, \tag{4.20}$$

where (t_1, t_2, n) is a local coordinate system with t_1 and t_2 being the two mutually orthogonal unit tangent vectors on a plane surface and n being a unit normal vector of the surface.

From (4.20) one sees an immediate difficulty in evaluating $\frac{\partial \phi}{\partial n}$. There is not enough information present to compute the normal derivative of the potential at the centroid of a panel based on the potentials at the panel vertices. One solution is to extract the surface tangential components of (4.19). That is:

$$\hat{t_1}[\int_{S_{nc}} ds' G_0(\overline{r}, \overline{r'}) \frac{\partial \overline{E}(\overline{r})}{\partial n} - (\int_{S_{nc}} + \int_{S_c}) ds' \frac{\partial G_0(\overline{r}, \overline{r'})}{\partial n} \overline{E}(\overline{r}) + \frac{1}{2} \overline{E}(\overline{r})] + \frac{\partial \phi(\overline{r})}{\partial t_1} = 0 \quad (4.21)$$

and

$$\hat{t_2}[\int_{S_{nc}} ds' G_0(\overline{r}, \overline{r'}) \frac{\partial \overline{E}(\overline{r})}{\partial n} - (\int_{S_{nc}} + \int_{S_c}) ds' \frac{\partial G_0(\overline{r}, \overline{r'})}{\partial n} \overline{E}(\overline{r}) + \frac{1}{2} \overline{E}(\overline{r})] + \frac{\partial \phi(\overline{r})}{\partial t_2} = 0. \quad (4.22)$$

According to boundary conditions (2.27), tangential electric fields E_{t_1} and E_{t_2} are assumed to be zeros on the contacts. Therefore the tangential electric fields in (4.21) and (4.22) vanish when field evaluations are made on the contacts. In addition, boundary condition (2.28) assumes that $\frac{\partial \overline{E}}{\partial n}$ is negligible on the contacts. Therefore terms involve $\frac{\partial \overline{E}}{\partial n}$ vanish as well when evaluations are made on the contacts. Furthermore, according to boundary condition (2.29), ϕ is constant on the contacts, therefore the $\frac{\partial \phi}{\partial t}$ terms also vanish from both equations when evaluations are made on the contacts. It can then be concluded that the tangential extractions of the second dyadic equation expressed in (4.21) and (4.22) are only significant when evaluations are made on the non-contact conductor surfaces.

A standard centroid collocation scheme can be utilized for the discretization of

(4.21) and (4.22). Consequently the following matrix equation is produced:

$$[A]\begin{bmatrix} \frac{\partial E_x}{\partial n} \\ \frac{\partial E_y}{\partial n} \\ \frac{\partial E_z}{\partial n} \\ E_x \\ E_y \\ E_z \\ C_l \\ C_r \\ \phi \end{bmatrix} = \begin{bmatrix} 0 \\ 0 \end{bmatrix}$$

with

$$A = \begin{bmatrix} T_{1x}P_0 & T_{1y}P_0 & T_{1z}P_0 & T_{1x}D_0 & T_{1y}D_0 & T_{1z}D_0 & T_{1L}D_{2_l} & T_{1R}D_{2_r} & A_{T1} \\ T_{2x}P_0 & T_{2y}P_0 & T_{2z}P_0 & T_{2x}D_0 & T_{2y}D_0 & T_{2z}D_0 & T_{2L}D_{2_l} & T_{2R}D_{2_r} & A_{T2} \end{bmatrix},$$

where $[T_{1x}, T_{1y}, T_{1z}]$ and $[T_{2x}, T_{2y}, T_{2z}]$ are six N^{NC} by N^{NC} matrices that are the extractions of the tangential components of the non-contact evaluation panels and their projections onto the global x, y and z coordinates. T_{1L} and T_{2L} are two N^{NC} by N^M matrices that are the projections of the left contact normal onto the tangential directions of the non-contact evaluation panels. Similarly, T_{1R} and T_{2R} are matrices containing the projections of the right contact normal onto the tangential directions of the evaluation panels.

Utilizing the centroid collocation scheme, the matrices in A are derived as:

$$P_{0_{ij}} = \int_{S_{nc_j}} dr' G_0(\overline{r}_{ic}, \overline{r'}) \tag{4.23}$$

$$D_{0_{ij}} = \begin{cases} \int_{S_{nc_j}} dr' \frac{1}{2} & \text{if i=j} \\ -\int_{S_{nc_j}} dr' \frac{\partial G_0(\overline{r}_{ic}, \overline{r'})}{\partial n(\overline{r'})} & \text{if i} \neq \text{j} \end{cases}$$

$$D_{2_{l_{ij}}} = -\int_{S_{cl}} dr' \frac{\partial G_0(\overline{r}_{ic}, \overline{r'})}{\partial n(\overline{r'})} W_j(\overline{r'}) \tag{4.24}$$

$$D_{2_{r_{ij}}} = -\int_{S_{cr}} dr' \frac{\partial G_0(\overline{r}_{ic}, \overline{r'})}{\partial n(\overline{r'})} W_j(\overline{r'}). \tag{4.25}$$

Matrices P_0 and D_0 contain $\overline{E}$ field and $\frac{\partial \overline{E}}{\partial n}$ field responses, respectively, measured at the centroid of each non-contact evaluation panel due to source distribution on each non-contact panel. Matrices D_{2_l} and D_{2_r} contain $\overline{E}$ field responses measured at the centroid of each non-contact panel due to source distributions on the left and right contacts, respectively. Both P_0 and D_0 are N^{NC} by N^{NC} matrices. Both D_{2_l} and D_{2_r} are N^{NC} by N^M matrices.

A_{T1} and A_{T2} are matrix operators that compute the surface tangential components of $\nabla\phi$ using a finite-difference scheme on the vertex potentials of a panel. Using the panel shown in Figure 4-1 as an example, tangent unit vectors t_1 and t_2 of this panel are formed by connecting the midpoints of the panel's sides. $\frac{\partial \phi}{\partial t_1}$ for the panel can then be discretized with a finite-difference scheme:

$$\frac{\triangle\phi}{\triangle t_1} = \frac{\phi_2 + \phi_3 - \phi 1 - \phi 4}{2|M_{14}M_{23}|} \tag{4.26}$$

A_{T1} denotes the resulting finite-difference matrix for the entire system of panel vertices. Similar procedure is used to produce the finite-difference matrix A_{T2} for the discretization of $\frac{\partial \phi}{\partial t_2}$.

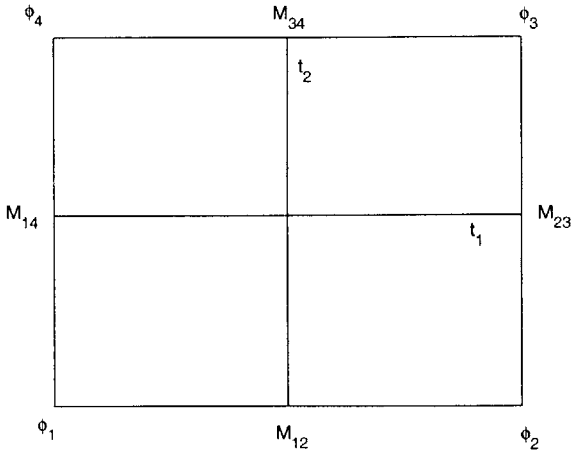

Figure 4-1: Discretization of $\frac{\partial \phi}{\partial t_a}$ (a=1 or 2).

4.3 Discretization of the scalar Poisson surface integral equation [16]

The scalar Poisson surface integral equation is given by (2.22). Substitute basis function(3.13) for ρ and basis function (3.16) for ϕ in (2.22) to obtain:

$$\sum_{j=1}^{N} \rho_j \int_{sj} ds' G_0(\overline{r}, \overline{r'}) - \varepsilon \sum_{j=1}^{N} \sum_{k=1}^{N} \frac{1}{4} \phi(v_{jk}) P_{cj}(\overline{r}) = 0. \tag{4.27}$$

It is worth noting at this point that both ρ and ϕ require the discretization of the entire conductor surface into regular quadrilateral panels. A centroid collocation scheme is then applied to generate a system of equations for the weights in (4.27). Consequently the following matrix equation is obtained:

$$P_0 \rho - \varepsilon A_p \phi_v = 0 \tag{4.28}$$

with

$$P_{0_{ij}} = \int_{S_j} ds' G_0(\overline{r}_{ic}, \overline{r'}), \tag{4.29}$$

where $\overline{r}_{ic}$ is the centroid of the ith evaluation panel and S_j is the surface of the jth source panel. A_P is a finite-difference matrix containing potential averaging coefficients that relate the potential at each panel centroid to the potential at its panel vertices.

Matrix P_0 is N by N, where N is the total number of discretized panels on the entire conductor surface. Matrix A_P is N by M, with M being the total number of panel vertices.

4.4 Discretization of the surface integral form of current conservation [16]

The purpose of the surface integral equation for current conservation in (2.24) is to resolve the electric potentials on the vertices of non-contact panels. As shall be seen in the next section, potentials on the vertices of the contact panels are resolved by

the boundary conditions in the formulation. For the sake of completeness, equation (2.24) is reiterated in this section as:

$$\int_c dc\,[E_t(\overline{r}) \cdot (n(\overline{r}) \times \ell(\overline{r}))] - \int_a da \frac{\partial E_n(\overline{r})}{\partial n(\overline{r})} = 0.$$

Consider a non-contact vertex O viewed as the centroid of a "dual" panel that is constructed by connecting the centroids of non-contact panels P_1,P_2,P_3 and P_4 surrounding O. As shown in Figure 4-2, this dual panel has area a and contour c. A discretized form of integral equation (2.24) can be formed by considering the part

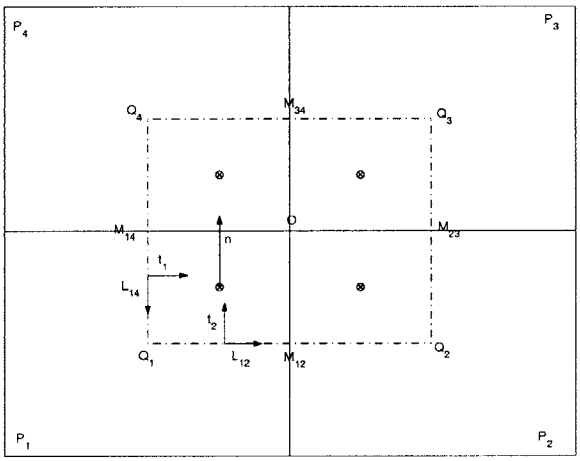

Figure 4-2: A dual panel

of each non-contact panel that contributes to a dual panel. Using panel P_1 as an example, subpanel $Q_1M_{12}OM_{14}$ is the part of P_1 that is used in the dual panel with M_{12} being the midpoint of the shared side between panels P_1 and P_2 and M_{14} being the midpoint of the shared side between panels P_1 and P_4.

Let's define $f_1(\overline{r})$ as the first line integral term of (2.24) applied to a dual panel with contour c, that is:

$$f_1(\overline{r}) = \int_c dc\,[E_t(\overline{r}) \cdot (n(\overline{r}) \times \ell(\overline{r}))]\,. \tag{4.30}$$

Now consider the contribution of panel P_1 to this integral. In particular, only subpanel $Q_1M_{12}OM_{14}$ of P_1 contributes to (4.30) with semgments $\overline{Q_1M_{12}}$ and $\overline{Q_1M_{14}}$ making up $\frac{1}{4}$ of the overall dual panel integration path. Furthermore, one sees from Figure

4-2 that ℓ_{12} is a unit vector in the direction of Q_1M_{12} and ℓ_{14} is a unit vector in the direction of Q_1M_{14}. With n being the unit surface normal vector of the panel, $n \times \ell_{14} = t_1$ is just a surface tangential vector along the direction of Q_1M_{12} and $n \times \ell_{12} = t_2$ is another surface tangential vector orthogonal to t_1 and situated along the direction of Q_1M_{14}. Therefore applying (4.30) to panel P_1 yields:

$$f_{1_{P1}}(\overline{r}) = \overline{E}(\overline{r}) \cdot (|Q_1M_{12}|t_1 + |Q_1M_{14}|t_2). \tag{4.31}$$

Substituting basis function (3.10) for the $\overline{E}$ field on the non-contact surfaces in (4.31) yields the discretized expression:

$$f_{1_{P1}} = (|Q_1M_{12}|t_{1x}+|Q_1M_{14}|t_{2x})E_x+(|Q_1M_{12}|t_{1y}+|Q_1M_{14}|t_{2y})E_y+(|Q_1M_{12}|t_{1z}+|Q_1M_{14}|t_{2z})E_z, \tag{4.32}$$

Now let's define $f_2(\overline{r})$ to be the dual panel area integral in (2.24), that is:

$$f_2(\overline{r}) = -\int_a da \frac{\partial E_n(\overline{r})}{\partial n(\overline{r})}. \tag{4.33}$$

Extracting from (4.33) the contribution of panel P_1, or more specifically, the contribution of subpanel $Q_1M_{12}OM_{14}$, results in the following expression:

$$f_{2_{P1}}(\overline{r}) = -\int_{a_{P1}} da \frac{\partial E_n(\overline{r})}{\partial n(\overline{r})}, \tag{4.34}$$

where a_{P1} is the surface area of subpanel $Q_1M_{12}OM_{14}$. It should be noted that $f_{2_{P1}}$ only accounts for $\frac{1}{4}$ of a dual panel area integration. Now substitute basis function (3.12) for $\frac{\partial \overline{E}}{\partial n}$ in (4.34). This yields the following discretized expression:

$$f_{2_{P1}} = (-a_{P1}n_x)\frac{\partial E_x}{\partial n} + (-a_{P1}n_y)\frac{\partial E_y}{\partial n} + (-a_{P1}n_z)\frac{\partial E_z}{\partial n}. \tag{4.35}$$

The discretized version of the surface integral form of current conservation for each non-contact panel is thus:

$$f_{1_{P1}} + f_{2_{P1}} = 0, \tag{4.36}$$

where $f_{1_{P1}}$ is defined in (4.32) and $f_{2_{P1}}$ is defined in (4.35). It should be noted that this sum only contributes to $\frac{1}{4}$ of the overall current conservation integral for a dual

panel. For the entire system of non-contact panels, the discretized form of current conservation can be expressed as the matrix equation:

$$C_x E_x + C_y E_y + C_z E_z + C_{dx}\frac{\partial E_x}{\partial n} + C_{dy}\frac{\partial E_y}{\partial n} + C_{dz}\frac{\partial E_z}{\partial n} = 0. \tag{4.37}$$

Matrices C_x, C_y, C_z, C_{dx}, C_{dy} and C_{dz} are all M^{NC} by N^{NC}, where M^{NC} is the number of non-contact vertices and N^{NC} is the number of non-contact panels. For the sake of matrix-size consistency, zeros are padded into the rows related to the contact vertices, thus expanding the matrices to M by N^{NC}, where M is the total number of panel vertices.

4.5 Discretization of boundary conditions

Equation (2.26) specifies the boundary condition for the non-contact conductor surfaces. Substitute basis functions (3.10) and (3.13) into boundary condition (2.26) for $\overline{E}$ and ρ, one obtains:

$$\sum_{j=1}^{N^{NC}} \left[(n_{x_j} E_{x_j} + n_{y_j} E_{y_j} + n_{z_j} E_{z_j}) = \frac{j\omega\rho_j}{\sigma} \right]. \tag{4.38}$$

The discretized form of (4.38) can be written as a matrix equation:

$$(N_{NC_x} E_x + N_{NC_y} E_y + N_{NC_z} E_z) - W_p = 0. \tag{4.39}$$

Matrices N_{NC_x}, N_{NC_y}, N_{NC_z} and W_p are all N^{NC} by N^{NC}, where N^{NC} is the number of non-contact panels.

Boundary conditions (2.27) and (2.28) for the contact surfaces are integrated within the formulation implementation itself. Therefore these equations do not need to be explicitly discretized.

Finally, according to boundary condition (2.29), constant potentials need to be applied to the panel vertices on the contacts. The discretized form of (2.29) is:

$$I_c \phi_v = \phi_c, \tag{4.40}$$

where matrix I_c specifies the contact panel vertices from the entire set of conductor panel vertices and ϕ_c sets those contact vertices to a certain positive or negative

potential depending on the polarity of the current applied to the contact. I_c is M by M with only M^c non-zero rows, where M^c is the number of panel vertices on the contacts and M is the total number of panel vertices over the entire conductor surface. ϕ_c is a vector of M elements with only M^c non-zero entries.

4.6 System formation

Under full-wave considerations, the discretized equations formulated in this chapter are assembled into a system matrix with $6N^{NC}$+$2N^M$+N+M equations and $6N^{NC}$+$2N^M$+N+M unknowns where N^{NC} is the number of non-contact panels, N^M is the number of conduction modes, N is the number of discretized panels over the entire conductor surface and M is the total number of vertices on those panels.

Let A=

$$\begin{bmatrix}
P & 0 & 0 & D & 0 & 0 & n_{l_x}L_l & n_{r_x}L_r & 0 & 0 \\
0 & P & 0 & 0 & D & 0 & n_{l_y}L_l & n_{r_y}L_r & 0 & 0 \\
0 & 0 & P & 0 & 0 & D & n_{l_z}L_l & n_{r_z}L_r & 0 & 0 \\
n_{l_x}J_l & n_{l_y}J_l & n_{l_z}J_l & n_{l_x}k_l & n_{l_y}k_l & n_{l_z}k_l & D_{ll} & (\hat{n}_l \cdot \hat{n}_r)D_{lr} & 0 & 0 \\
n_{r_x}J_r & n_{r_y}J_r & n_{r_z}J_r & n_{r_x}k_r & n_{r_y}k_r & n_{r_z}k_r & (\hat{n}_r \cdot \hat{n}_l)D_{rl} & D_{rr} & 0 & 0 \\
T_{1x}P_0 & T_{1y}P_0 & T_{1z}P_0 & T_{1x}D_m & T_{1y}D_m & T_{1z}D_m & T_{1L}D_{2_l} & T_{1R}D_{2_r} & A_{T1} & 0 \\
T_{2x}P_0 & T_{2y}P_0 & T_{2z}P_0 & T_{2x}D_m & T_{2y}D_m & T_{2z}D_m & T_{2L}D_{2_l} & T_{2R}D_{2_r} & A_{T2} & 0 \\
0 & 0 & 0 & 0 & 0 & 0 & 0 & 0 & \varepsilon A_p & P_0 \\
0 & 0 & 0 & N_{NC_x} & N_{NC_y} & N_{NC_z} & 0 & 0 & 0 & W_p \\
C_{d_x} & C_{d_y} & C_{d_z} & C_x & C_y & C_z & 0 & 0 & I_c & 0
\end{bmatrix},$$

then

$$[A]\begin{bmatrix} \frac{\partial E_x}{\partial n} \\ \frac{\partial E_y}{\partial n} \\ \frac{\partial E_z}{\partial n} \\ E_x \\ E_y \\ E_z \\ C_l \\ C_r \\ \phi \\ \rho \end{bmatrix} = \begin{bmatrix} 0 \\ 0 \\ 0 \\ 0 \\ 0 \\ 0 \\ 0 \\ 0 \\ I_c \\ 0 \end{bmatrix}.$$

The first five rows of Matrix A correspond to the discretized first dyadic integral equation. The next two rows correspond to the discretized second dyadic integral equation. The eigth row is the discretized Poisson potential integral equation. The ninth row corresponds to the discretized non-contact surface normal boundary condition. The tenth row contains two discretized equations: the integral equation for current conservation applied to the vertices of non-contact panels and the potential boundary condition applied to the vertices of contact panels.

The unknown vectors $\frac{\partial E_x}{\partial n}$, $\frac{\partial E_y}{\partial n}$ and $\frac{\partial E_z}{\partial n}$ are the weights of the piecewise-constant basis functions for the normal derivative of the electric field on the non-contact panels. Vectors E_x, E_y and E_z are the weights of the piecewise-constant basis functions for the electric fields on the non-contact panels. Vector C_l and C_r contain the weights of the conduction mode basis functions used to represent the electric field on the left and right contacts, respectively. Vector ρ is the weights of the piecewise-constant basis functions for the surface charge densities over the entire conductor surface and vector ϕ specifies the weights of the basis functions representing the electric potentials over the entire conductor surface.

Even though the formulation described in the paper is implemented under full-wave assumptions, the equations in the formulation can be easily modified to accomodate magneto-quasistatic (MQS) conditions. In particular, under MQS assumptions,

charge density ρ becomes zero. Therefore ρ is eliminated from the formulation as an unknown. Likewise, the scalar Poission integral equation is eliminated from the formulation. Furthermore, MQS normal boundary condition for non-contact panels is used, that is, $E_n = 0$ on non-contact surfaces. Overall, the system matrix is reduced to a size of $6N^{NC}$+$2N^{M}$+M by $6N^{NC}$+$2N^{M}$+M.

Matrix B is the system matrix generated under MQS assumptions with B=

$$\begin{bmatrix}
P & 0 & 0 & D & 0 & 0 & n_{l_x}L_l & n_{r_x}L_r & 0 \\
0 & P & 0 & 0 & D & 0 & n_{l_y}L_l & n_{r_y}L_r & 0 \\
0 & 0 & P & 0 & 0 & D & n_{l_z}L_l & n_{r_z}L_r & 0 \\
n_{l_x}J_l & n_{l_y}J_l & n_{l_z}J_l & n_{l_x}k_l & n_{l_y}k_l & n_{l_z}k_l & D_{ll} & (\hat{n_l}\cdot\hat{n_r})D_{lr} & 0 \\
n_{r_x}J_r & n_{r_y}J_r & n_{r_z}J_r & n_{r_x}k_r & n_{r_y}k_r & n_{r_z}k_r & (\hat{n_r}\cdot\hat{n_l})D_{rl} & D_{rr} & 0 \\
T_{1x}P_0 & T_{1y}P_0 & T_{1z}P_0 & T_{1x}D_m & T_{1y}D_m & T_{1z}D_m & T_{1L}D_{2_l} & T_{1R}D_{2_r} & A_{T1} \\
T_{2x}P_0 & T_{2y}P_0 & T_{2z}P_0 & T_{2x}D_m & T_{2y}D_m & T_{2z}D_m & T_{2L}D_{2_l} & T_{2R}D_{2_r} & A_{T2} \\
0 & 0 & 0 & N_{NC_x} & N_{NC_y} & N_{NC_z} & 0 & 0 & 0 \\
C_{d_x} & C_{d_y} & C_{d_z} & C_x & C_y & C_z & 0 & 0 & I_c
\end{bmatrix}.$$

4.7 Current computation and impedance extraction

Under the assumption of a two-ported conductor system operating at a certain frequency f with a potential difference V_{diff} applied between the two terminals of the conductor, the current flowing through each contact terminal can be computed after solving the system matrix in the above section for the unknowns. For example, the current through the left contact can be evaluated using (2.30). Substitute the conduction mode basis function representation for contact surface E_n in (2.30) yields:

$$\overline{I}_{cl} = \hat{n}_l \sigma \sum_{j=1}^{N^M} \int_{s_{cl}} dr C_{l_j} W_j(\overline{r}), \tag{4.41}$$

where W's are the conduction mode basis functions, $\hat{n}_l$ is the left contact normal, and C_l are weights of the left contact conduction mode basis functions obtained from solving the system matrix.

Given the dimension of the left contact, each integral in the above summation can be evaluated analytically to obtain the net current flow through the left contact. Once the contact current is known, the impedance of the conductor at each frequency can be computed using (2.31),(2.32) and (2.33).

In contrast to our implementation of using a consistent method of computing contact current, FastImp switches between two different methods of computing contact current depending on the skin depth. At low frequencies where skin depth is greater than the width of the conductor contact, FastImp uses (2.30) to determine current flow through each contact by utilizing the weights of the piecewise constant basis function representing the contact E_n field. However, At high frequencies where the skin depth is less than the contact width, the exponential variation in E_n cannot be accurately represented by the piecewise constant basis functions without using a much refined discretization on the contacts. For this reason FastImp uses a different method of computing contact current that involves a line integration along the contour of a cross section near the contact. That is:

$$\overline{I} = \frac{\sigma}{\sigma + i\omega E} \frac{-1}{i\omega\mu} \int_L dl \left(\nabla \times \overline{E}(r) \right) \cdot t_l, \tag{4.42}$$

where $\hat{t}_l$ is the unit vector along the closed contour L on the non-contact surfaces. Therefore, the non-contact surfaces must now be discretized finely in order to ensure that the skin and proximity effects are captured at high frequencies.

As one can see, the new method presented in this thesis offers consistency in computing contact current over a wide range of frequencies while the method in FastImp does not. The relative accuracy and efficiency of these two methods are determined in the next chapter.

Chapter 5

Computational results

This section presents some of the computational results obtained from the new method of evaluating contact current. Specifically, impedance extraction results for a straight wire, a ring conductor and a transmission line are presented in this chapter to validate the accuracy and efficiency of the new method introduced in the thesis. It should be noted that since the algorithm is implemented in MatLab, the size and the complexity of the examples are rather limited.

For the wire and the ring examples, result comparisons are made with FastImp and the magnetoquasistatic analysis program FastHenry. Therefore these examples are analyzed magnetoquasistaticly for the sake of performance comparison with FastHenry. For the transmission line example, electromagneto-quasistatic analysis is performed by both FastImp and our conduction mode method. In general, full-wave solves are also possible.

5.1 A straight wire

Consider a straight wire with a square cross-section of $10\mu m$ by $10\mu m$ and a length of $100\mu m$. The conductivity of the wire is that of copper which is $5.8 \times 10^7 \frac{S}{m}$. Impedance extractions are performed under applied frequencies ranging from 1Hz to 10GHz.

In FastImp, the surface of this conductor is uniformly discretized with 4X4 panels on each contact and 4X6 panels on each of the four non-contact faces along the length

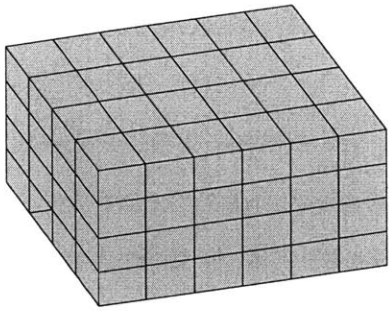

Figure 5-1: A discretized wire structure

of the conductor as shown in 5-1. In the new method, the same 4X6 discretization on each non-contact face of the conductor is used. As for the contacts, either $\frac{1}{2}$ or $\frac{1}{4}$th of a contact is treated as a support for each of the 8 conduction modes.

Since FastImp uses the contours near the contacts to evaluate contact current at high frequencies, the non-contact surface discretization needs to have panels as small as a skin depth. With a uniform discretization of 4 panels per face along the contour of the contacts, the dimension of each panel quickly exceeds skin depth as operating frequencies increase. In order to ensure that panel dimensions remain within $\frac{1}{8}$th of a skin depth at the highest frequency of 10GHz one would need to use a 12X12X6 non-uniform discretization. This discretization generates 12X12 panels on the contacts and 12X6 panels on each face along the conductor length. Results obtained from this fine discretization are used to compare to results from our conduction mode method of only 4X4X6 coarse non-contact surface discretization. That is 4x6 panels on the non-contact faces and 8 conduction modes on each contact face.

Finally, FastHenry is run on the same conductor structure with 324 filaments so that the cross-section of the smallest filament is within $\frac{1}{8}$th of the skin depth at even the highest frequency used in this example. The solution obtained from such fine volume discretization can be safely assumed to be accurate and can be used as a reference for validation purposes.

5.1.1 Accuracy

For excitation frequencies within the range of 1Hz to 10MHz, where skin effects are not significant, the wire resistances are expected to be close to that of the DC value, which is obtained analytically to be 0.017241Ω for this structure. From the resistance comparison plot in Figure 5-2, one can conclude that results from FastImp's coarse and fine discretizations and from our conduction mode method are all accurate in comparison to this DC resistance value. However, our conduction mode method offers more accurate evaluations of inductances. Inductances are expected to be constant at low frequencies. Based on such observation, the inductance analysis shown in Figure 5-3 reveals that this is clearly not the case for the FastImp method with both coarse and fine discretizations. Our conduction mode method has a maximum error of 1% from FastHenry's inductance at 100Hz. On the other hand, inductance from FastImp's coarse discretization has an error of 30% at the same frequency, and inductance from its fine discretization has an error of 61%.

When compared to FastHenry at high frequencies, our method with the coarse 4X4X6 non-contact surface discretization yields similar resistance accuracy as FastImp's fine non-uniform 12X12X6 discretization. Results from FastImp's non-uniform fine discretization are expected to be accurate since the discretization ensures that the dimension of each panel is small enough compare to skin depth at all frequencies used. FastImp's coarse 4X4X6 discretization shows a degraded resistance performance. At the maximum frequency of 10GHz, resistances from both our method and FastImp's fine discretization scheme deviate within 1% of the "accurate" solution generated by FastHenry. FastImp's coarse discretization deviates by 5%.

5.1.2 Cost

In this example, our conduction mode method uses 96 non-contact panels. FastImp generates 128 panels using the 4X4X6 coarse discretization, 32 of which are contact panels. FastImp produces 1152 panels using the 12X12X6 fine discretization, 288 of which are contact panels. In general, our method uses fewer panels while providing

the most accurate solution at low frequencies. At high frequencies, despite the fact that our method uses 12 times fewer panels than FastImp's fine discretization scheme, results from our method have comparable accuracy to FastImp's fine discretization results and are more accurate than FastImp's coarse discretization results that uses 32 more panels than our method. The sizable discrepancy in cost between our conduction mode method and FastImp's non-uniform fine discretization scheme is due to that the fact that our conduction mode method has removed the constraint of fine discretization on the non-contact surfaces in order to achieve high accuracy in results. In fact, our conduction mode method uses a factor of 9 times fewer non-contact surface panels compare to FastImp's fine discretization scheme.

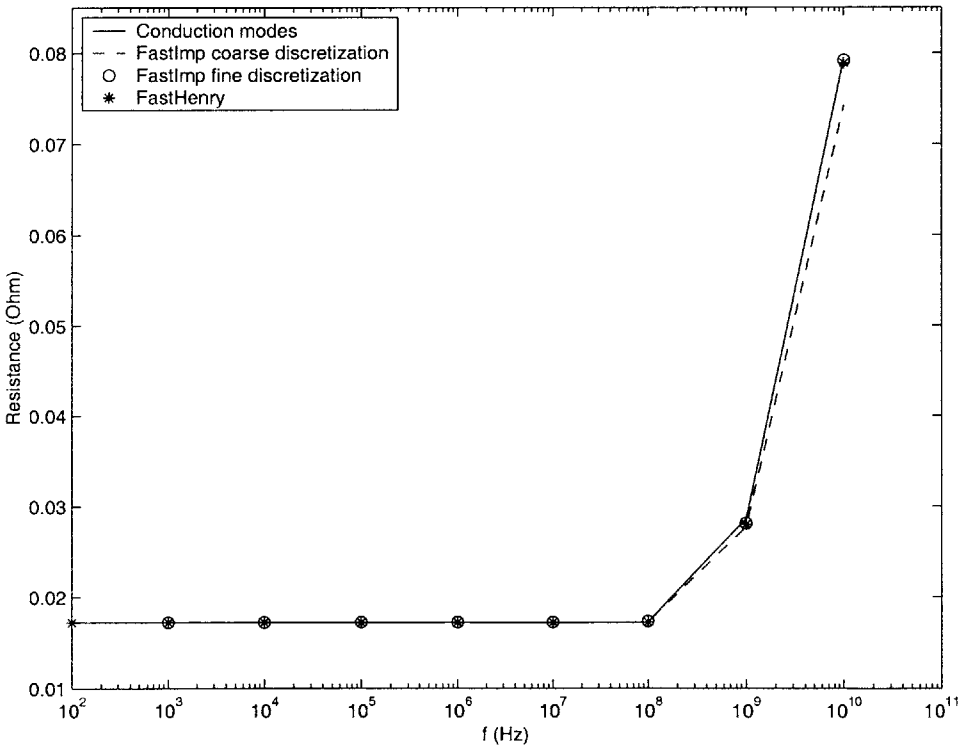

Figure 5-2: Resistance of the wire

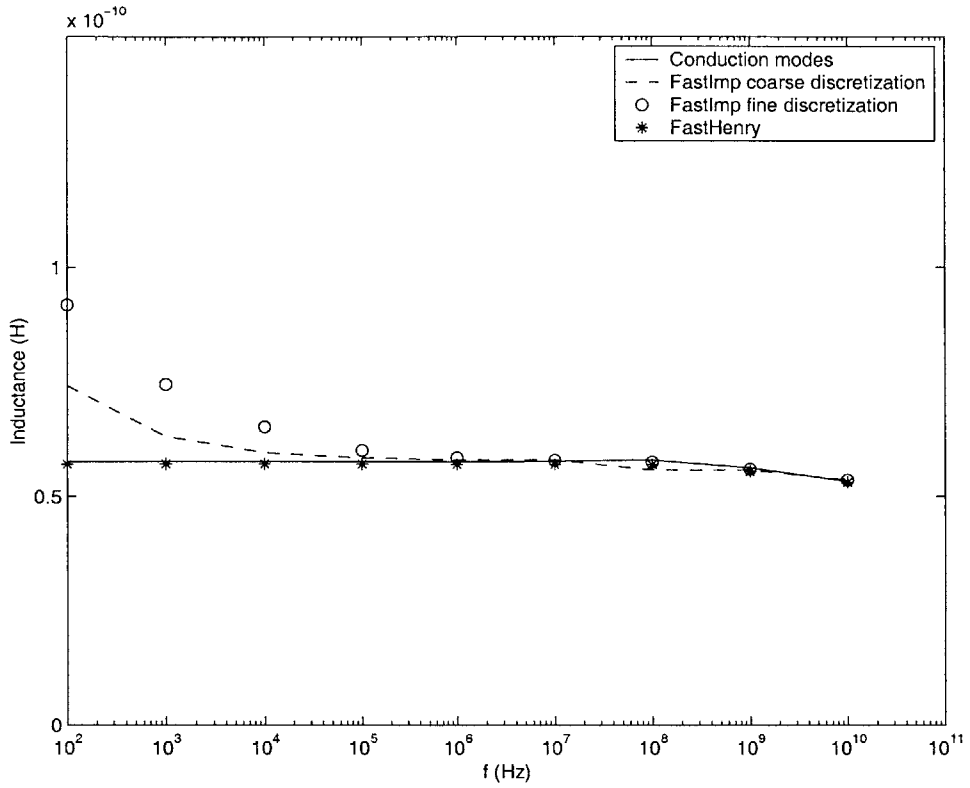

Figure 5-3: Inductance of the wire

5.2 A ring

Consider a ring as shown in Figure 5-4 with an inner radius of $20\mu m$ and a square cross-section of $10\mu m$ by $10\mu m$. In FastImp, the structure of this ring is discretized uniformly into 4X4 panels on each contact and 4X8 panels on each of the four non-contact faces along the curved length of the conductor. For the conduction mode basis function method, the same 4X8 discretization on each non-contact face of the conductor is used. FastImp is again run on the ring structure with a 12X12X8 fine non-uniform surface discretization so that the length of the smallest panel is within $\frac{1}{8}$th of the smallest skin depth used. FastHenry is run on the same ring with a 1568-filament volume discretization. The cross-section of the smallest filament is within $\frac{1}{4}$th of the smallest skin depth used.

For this ring structure, impedance extractions are performed under applied frequencies ranging from 1Hz to 30GHz. It should be noted that since this structure

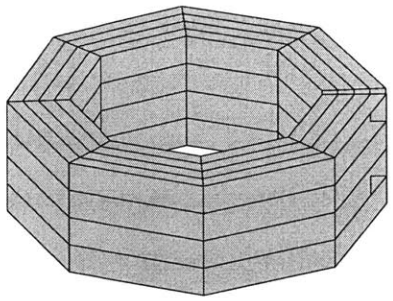

Figure 5-4: A discretized ring structure

is larger and more complex then the straight wire example, discrepancies between the results produced by our conduction mode method and FastImp will be more pronounced.

5.2.1 Accuracy

At low frequencies, Figure 5-6 demonstrates that our method provides the best inductance evaluations with a maximum error of 9% at 100Hz while FastImp's coarse discretization yields an error of 32% and its fine discretization yields an error of 30% at the same frequency.

From Figure 5-5, one observes that at high frequencies, resistances produced by either our method or FastImp's fine discretization method show a large discrepancy compare to resistances produced by FastImp's coarse discretization. Assuming that FastHenry's solution is the "accurate" solution, then the resistances produced by our method show a maximum deviation of 4% occurring at 30GHz. The resistances produced by FastImp's fine discretization have a maximum deviation of 4% as well. In contrast, FastImp's coarse discretization results show a maximum 16% deviation at the same frequency.

More importantly, one observes that both set of FastImp's solutions show a noticeable dip in resistance at 100MHz as seen in Figure 5-5. This dip is due to FastImp's switching between two different methods of computing contact current as frequencies transition from low to high, which occurs around 100MHz. Our surface conduction

mode basis function method has evidently corrected this discontinuity in solution by implementing one consistent method of computing contact current.

At high frequencies, it has been demonstrated in Figure 5-6 that inductances from both our method and from FastImp's fine discretization scheme deviate at most 2% from FastHenry's inductance at 30GHz while inductance from FastImp's coarse discretization deviates 13% at the same frequency.

5.2.2 Cost

Our conduction mode method uses 128 discretized panels. FastImp uses 160 panels in its 4X4X8 coarse discretization scheme, 32 of which are contact panels. FastImp uses 1440 panels in its 12X12X8 fine discretization scheme, 288 of which are contact panels. In general, our method uses fewer panels than FastImp, yet yielding the most accurate results at low frequencies. At high frequencies, our method uses a factor of 12 times fewer panels than FastImp's fine discretization scheme, yet still managing to provide results with comparable accuracy. FastImp's coarse discretization with 32 more panels than our method fares much worse in terms of accuracy.

5.3 Transmission Line

The goal of this example is to test the ability of our conduction mode method to capture wavelength-related resonance phenomena under the influence of skin effects and proximity effects. In this simulation, two typical IC package wires, each 1cm long with $10\mu m$ by $40\mu m$ on the cross section, are situated $10\mu m$ apart. Worst case high-Q resonances are obtained when the two wires are shorted at one end and are excited with an ideal voltage source as shown in 5-7. When the excitation frequency is such that the length of the transmission line is close to a quarter or a half of the wavelength, one may observe sharp resonance peaks as shown in Figure 5-8. The amplitude of such peaks is mainly determined by skin and proximity effects.

It should be noted that both FastImp and our conduction mode method conducted EMQS analysis on this transmission line structure. First, we ran our conduction mode

method using a 2X10 and 3X10 coarse discretization along the non-contact faces of the two wires with 8 conduction modes on each contact face. To produce an accurate reference solution using the original FastImp approach we ran a second experiment where we had to use on the contact faces a fine 8x9 non-uniform discretization in order to produce panels of about one skin depth. In the original FastImp approach such discretization implies a similar fine discretization on the non-contact panels near the contacts and therefore along the entire wire length. In order to avoid long and skinny panels that cannot be efficiently handled by PFFT, a minimum of 35 sections along the length must then be used, thereby producing a very large number of unknowns even for this very simple problem.

5.3.1 Accuracy

In Figure 5-10, The conduction mode method gives a worst-case 3.4% error in the position of the first quarter-wavelength impedance resonance when compared to the reference fine discretization solution. A worst-case error of 3.2% is measured on the impedance amplitude of the same resonance. The discrepancies in resonance amplitude are more evident in Figure 5-9.

5.3.2 Cost

In this transmission line example, our conduction mode method uses a total of 200 panels. FastImp's coarse discretization scheme generates a total of 224 panels and FastImp's fine discretization scheme generates 2668 panels. With even fewer number of panels than FastImp's coarse discretization, the conduction mode method is able to reach within 5% accuracy to FastImp's fine discretization method that uses 13 times more panels than the conduction mode method. It is evident that the majority of the savings in cost of our conduction mode method in comparison to FastImp's fine discretization scheme is due to the use of much fewer panels on the non-contact surfaces, more specifically, a factor of 12 times fewer. We can finally realize that the factor of 12 reduction applies to tightly interacting panels. Since such panels do not

exploit the PFFT acceleration, the final save in memory and time is a square factor of $12^2 = 144$.

5.4 Conclusion

A number of conclusions can be drawn from the above results. One is that the conduction modes, originally developed in [2] for a volume integral method can be applied to a surface integral method. Furthermore, these basis functions can be modified by confining their coverage to certain areas on a contact so as to promote their linear independence while still maintaining their effectiveness.

It has been determined that using these modified conduction modes as basis functions on the contacts offers improvements in the accuracy of conductor impedance evaluation when compared with the existing approach in FastImp. More specifically, at high frequencies, our conduction mode basis functions is more effective in taking into account skin effects. At low frequencies, improvements in inductances are observed due to the use of the Galerkin technique in field evaluations from the contact surfaces.

It has also been observed that in order to capture skin and proximity effects, the original FastImp needs to use a very fine discretization on contact faces which implies a similarly fine discretization on non-contact faces in order to avoid high aspect ratios on tightly interacting panels which are unfavorable for PFFT. For the same final accuracy in a transmission line example, by using only up to eight conduction modes as basis functions on the contacts, we could use a 12 times coarser discretization of the non-contact surfaces. Therefore a saving factor of 144 in memory and simulation time can be achieved with the new method.

Finally, it should be noted that FastImp utilizes different techniques for computing contact current at different frequencies. In FastImp, a switch of evaluation method is made when the skin depth becomes smaller than the length of the contact. In contrast, our improved method offers a consistent technique for evaluating contact current and conductor impedance at every frequency level.

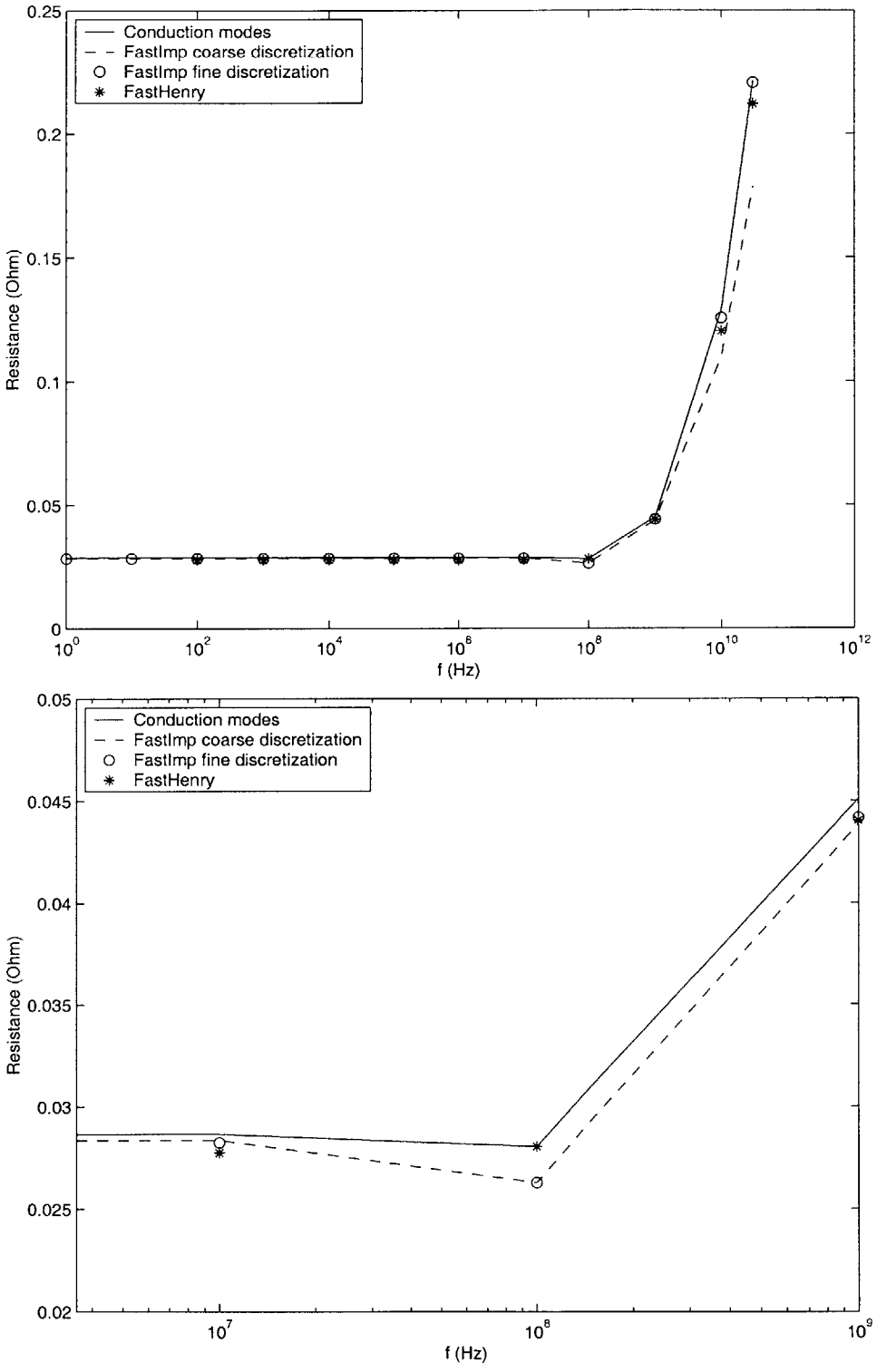

Figure 5-5: Resistance of the ring with a closer view of the "dip" in FastImp's results occurring at 100MHz due to the switching of contact current evaluation method.

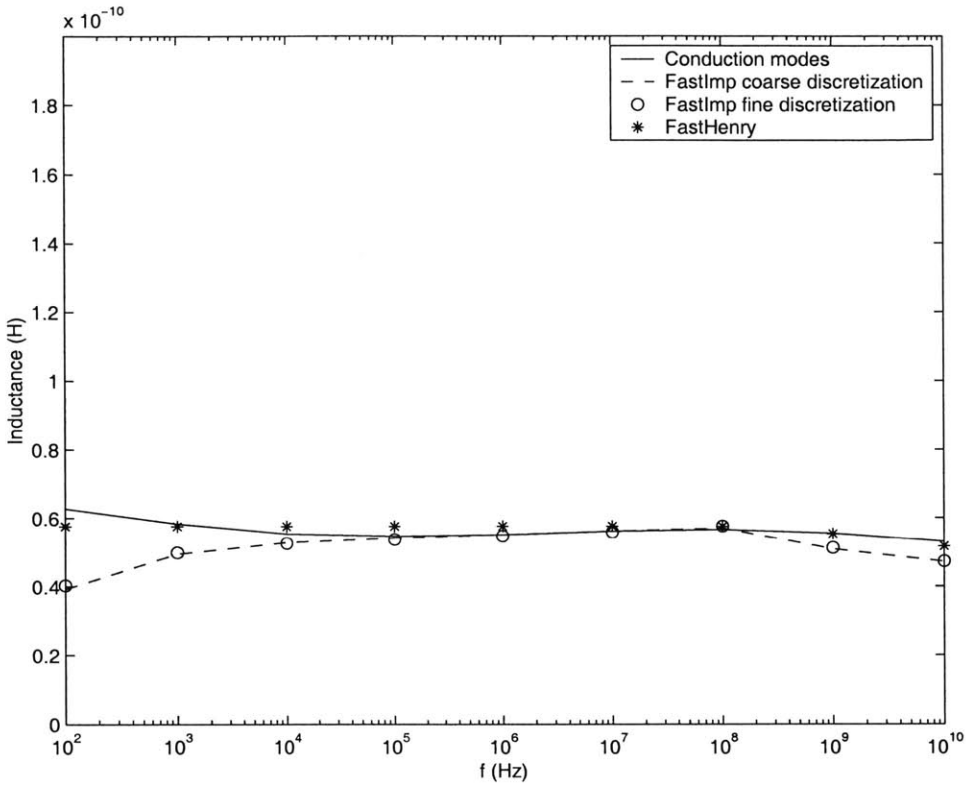

Figure 5-6: Inductance of the ring

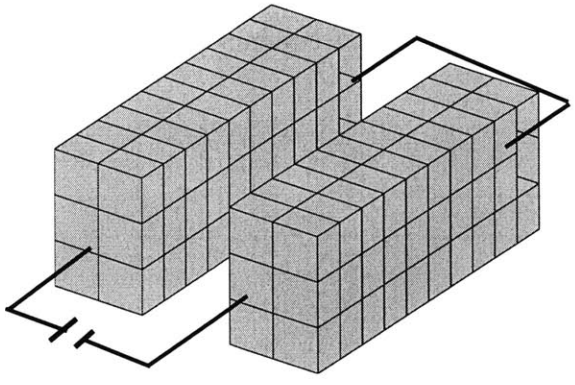

Figure 5-7: A discretized transmission line structure

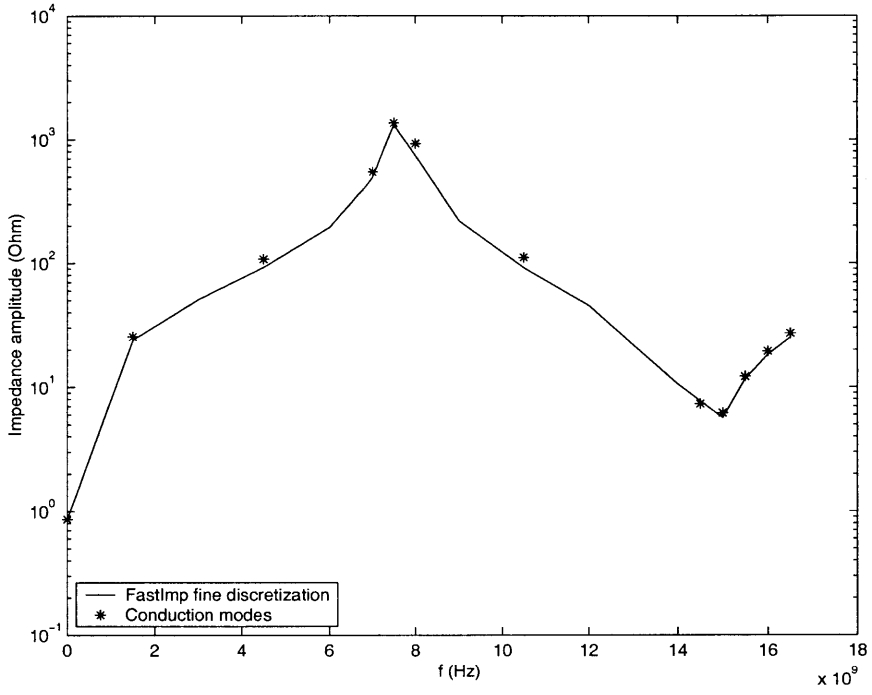

Figure 5-8: Impedance amplitude vs. frequency for a shorted T-line plotted on a log amplitude scale.

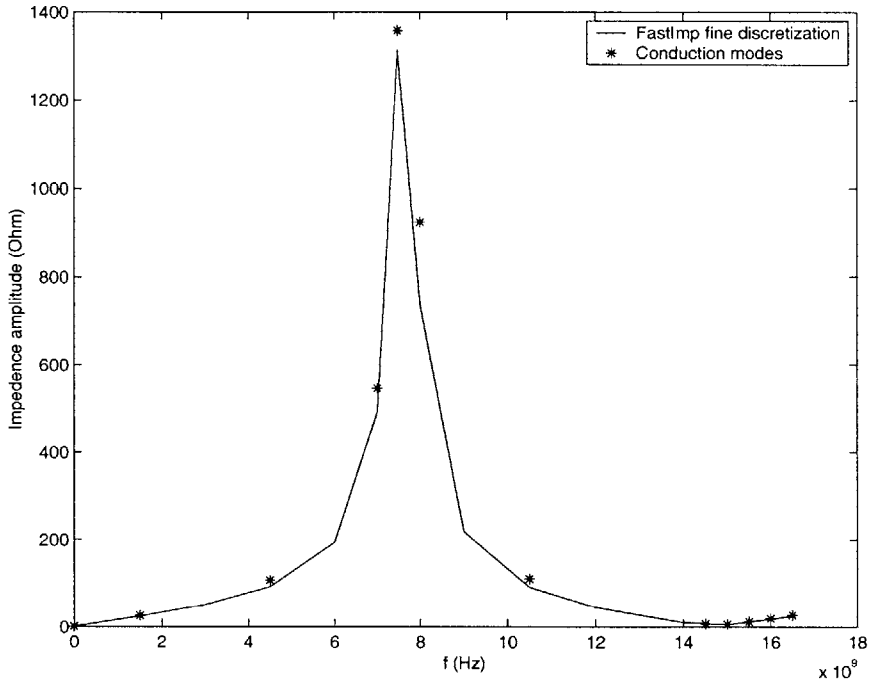

Figure 5-9: Impedance amplitude vs. frequency for a shorted T-line plotted on a linear amplitude scale.

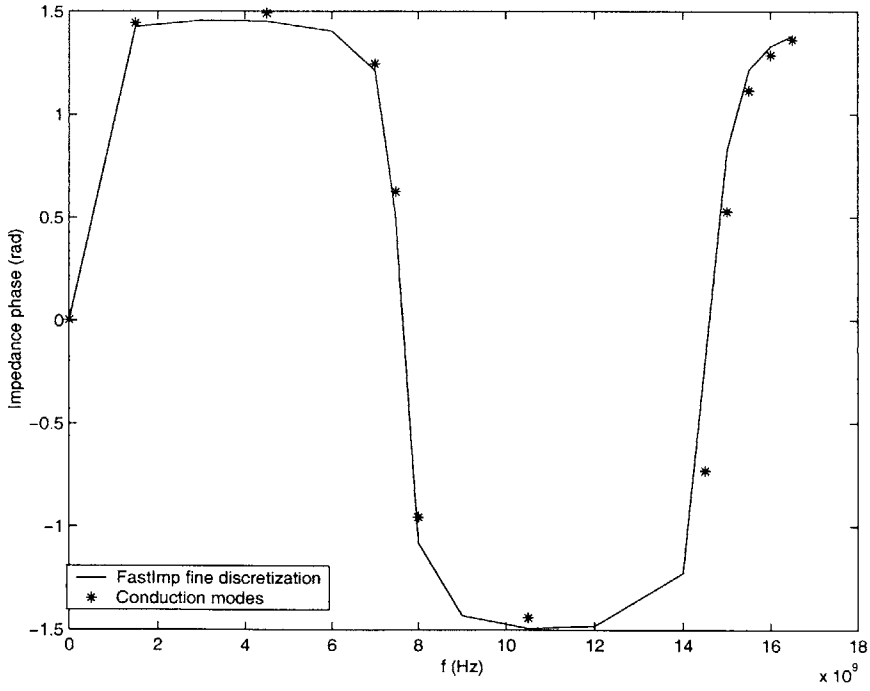

Figure 5-10: Impedance phase vs. frequency for a shorted T-line.

Bibliography

[1] Z. Zhu, J. Huang, B. Song and J. White. "Algorithms in FastImp: A fast and wideband impedance extraction program for complicated 3D geometries." *Proceedings of IEEE/ACM Design Automation Conference*, San Diego, California, June 2-6 2003.

[2] L. Daniel, A. Sangiovanni-Vincentelli, and J. White. Using conduction modes basis functions for efficient electromagnetic analysis of on-chip and off-chip interconnect. In *Design Automation Conference*, June 2001.

[3] D. Ling and A.E. Ruehli. *Circuit Analysis, Simulation and Design.* Elsevier Science Publishers B. V., North-Holland, 1987.

[4] Y. Massoud and J.K. White. "Simulation and Modeling of the Effect of Substrate Conductivity and Coupling Inductance." *Proceedings of the International Electronic Devices Meeting,* Washington D.C., pp.491-494, December 1995.

[5] K. Nabors and J.K. White. "FASTCAP: A Multipole-Accelerated 3-D Capacitance Extraction Program." *IEEE Trans. on Computer-Aided Design,* vol.10, pp. 1447-1459, Nov. 1991.

[6] M. Kamon, M.J.Tsuk and J.K. White. "Fasthenry: A Multipole-Accelerated 3-D Inductance Extraction Program." *IEEE Trans. on Microwave Theory and Techniques,* vol. 42, no.9, pp. 1750-1758, Sep. 1994.

[7] W. T. Weeks, L. L. Wu, M. F. McAllister, and A. Singh. Resistive and inductive skin effect in rectangular conductors. *IBM J. Res. Develop.*, 23(6):652–660, November 1979.

[8] P. Silvester. Modal network theory of skin effect in flat conductors. *Proc. IEEE*, 54(9):1147–1151, September 1966.

[9] M. J. Tsuk and J. A. Kong. A hybrid method for the calculation of the resistance and inductance of transmission lines with arbitrary cross section. *IEEE Trans. on Microwave Theory and Techniques*, 39(8):1338–1347, August 1991.

[10] K. M. Coperich, A. E. Ruehli, and A. Cangellaris. Enhanced skin effect for partial-element equivalent-circuit (peec) models. *IEEE Trans. on Microwave Theory and Techniques*, 48(9):1435–42, September 2000.

[11] Y. Saad and M.H. Schultz. "GMRES: A Generalized Minimal Residual Algorithm for Solving Nonsymmetric Linear Systems." *SIAM Journal on Scientific and Statistical Computing,* 7:856-869. July,1986.

[12] J.R. Phillips and J.K. White. "A Precorrected-FFT Method for Electrostatic Analysis of Complicated 3-D structures." *IEE Trans. Computer-Aided Design,* pp.1059-1072, 1997.

[13] J. Tausch and J.K. White. "Wavelet-like Bases for Integral Equations on Surfaces with Complex Geometry." *IMACS Series in Computational and Applies Mathematics,* IMACS, 1998.

[14] J. Kong. *Electromagnetic Wave Theory.* EMW Publishing, Cambridge, MA, 2000.

[15] Chen-to Tai. *Dyadic Green functions in Electromagnetic Theory.* IEE Press, Piscataway, NY, 1994.

[16] J. Wang. *A New Surface Integral Formulation of EMQS Impedance Extraction for 3-D Structures.* Ph.D. thesis, MIT EECS Department, 1999.

[17] H.A. Haus and J.R. Melcher *Electromagnetic Fields and Energy.* Prentice-Hall, Englewood Cliffs, NJ, 1989.

[18] R. F. Harrington. Field Computation by Moment Methods. *MacMillan*, New York, 1968.